A unified hybrid lattice-Boltzmann method for compressible flows: Bridging between pressure-based and density-based methods

G. Farag, T. Coratger, G. Wissocq, S. Zhao, Pierre Boivin, P. Sagaut

A unified hybrid lattice-Boltzmann method for compressible flows: bridging between pressure-based and density-based methods

G. Farag,[1, a)] T. Coratger,[1] G. Wissocq,[1] S. Zhao (赵崧),[1] P. Boivin,[1, b)] and P. Sagaut[1]

Aix Marseille Univ, CNRS, Centrale Marseille, M2P2, Marseille,

France

(Dated: July 20, 2021)

A unified expression for high-speed compressible segregated consistent lattice Boltzmann methods, namely pressure-based and improved density-based methods, is given. It is theoretically proved that in the absence of forcing terms these approaches are strictly identical and can be recast in a unique form. An important result is that the difference with classical density-based methods lies in the addition of fourth-order term in the equilibrium function. It is also shown that forcing terms used to balance numerical errors in both original pressure-based and improved density-based methods can be written in a generalized way. A hybrid segregated efficient lattice-Boltzmann for compressible flow based on this unified model, equipped with a recursive regularization kernel is proposed and successfully assessed on wide set of test cases with and without shock waves.

[a)]Electronic mail: gabriel.farag@live.fr

[b)]Electronic mail: pierre.boivin@univ-amu.fr

I. INTRODUCTION

The derivation of efficient Lattice-Boltzmann Methods for compressible flows or flows with complex thermodynamics (e.g. phase change, combustion, complex equation of state ...) is a research topic that has been investigated intensively during the last two decades[1,2]. Among the key issues raised by these extensions one can mention: accounting for the equation of state, which governs the pressure gradient in the associated macroscopic momentum equation, coupling with the energy equation and handling flows with discontinuities or very strong gradients.

Most existing methods belong to the class of density-based methods, i.e. they are such that the zeroth-order moment of the distribution functions f_i is equal to the fluid density $\sum_i f_i = \rho$. They are naturally obtained considering the truncation of direct expansion of the continuous Maxwellian onto Hermite polynomial basis[3]. These methods have been observed to be very efficient for low-Mach athermal flows[4–8], their use for the type of flows mentioned above is much less satisfactory, since both robustness and accuracy issues have been reported in several cases. This is especially true for high speed supersonic flows and multiphase flows with high density ratio. Several other ways to design a consistent and stable lattice-Boltzmann (LB) scheme have been proposed in the past, mostly by adding some source terms to balance some effects of the error. While such fixes enhance the range of reliability of the methods, they do not lead to very robust schemes well suited for a broad range of applications.

A way to improve the stability of the methods while keeping an expression of the collision kernel close to the classical density-based one is to switch to pressure-based methods, in which the zeroth-order moment of the density functions is the pressure instead of the density $\sum_i f_i = p/c_s^2$. These methods have been proposed initially for low-Mach reactive flows[9,10] and rapidly extended to low-Mach multiphase flows[11,12], but only very recently to high-speed compressible[13] and reactive flows[14,15] and to humid air thermodynamics[16]. A possible explanation for their efficiency has been very recently proposed[17] through theoretical analysis. The key point is that using an athermal 3rd order equilibrium moment and a different strategy for the force corrective term, they allow for the recovery of Lax-type convergence when performing grid refinement. They still require the use of forcing terms to balance some parts of the numerical error to be able to preserve accuracy at high Mach number, but the key difference is that they ensure robust solutions. A drawback of classical pressure-based methods is that they appear as predictor-corrector-type methods, the density being updated in the corrector step. This formulation may preclude the

straightforward use of some advanced crucial numerical elements, such as the direct coupling approach[18] for grid transition which has been observed to be a mandatory element for aeroacoustics.

Another way to improve the robustness of the density-based methods is to modify the expression of the equilibrium functions by inserting an *ad hoc* source term, whose zeroth-order moment is null, allowing for the preservation of the relation $\sum_i f_i = \rho$. Such an approach was proposed a long time ago for multiphase flows[19,20] and very recently applied to high-speed compressible flows[21], leading to the definition of improved density-based methods. A significant gain with respect to original density-based methods was reported in[21], but a full theoretical rationale for this gain was not provided.

The purpose of the present article is twofold. First, it is proved by theoretical analysis in Section II that segregated pressure-based and improved density-based regularized collision models are strictly identical in the absence of forcing terms, and therefore can be interpreted as implementation variants of the the same method, which can be written as a density-based method that does not rely on a predictor-corrector algorithm. The use of forcing terms to partially balance the numerical error is then considered. A unified general formulation that encompasses both segregated pressure-based and density-based along with forcing terms is then given in Section III. An important associated result is that differences between preexisting classical density-based, pressure-based and improved density-based methods simply lies in different third and fourth order equilibrium moments. An entropy equation is used to close the system, as in[13,22–24], whose finite-difference discretization is discussed in Section III. An optimal formulation of the correction forcing terms is proposed.

The unified method, which then appears as a modified density-based method, is assessed considering a wide set of test cases in Section IV. Conclusions are given in Section V.

II. HYBRID RECURSIVE REGULARIZED LATTICE BOLTZMANN MODELS

In this section, we thoroughly compare the p-based and improved ρ-based models applied to a regularized kernel. First, we perform a comparison of the pure LB schemes without forcing term. Specifying the equation of state (EOS) is unnecessary at this point as long as the compared schemes employed the same strategy, which is our assumption in what follows. Therefore, for the sake of generality, the normalized temperature $\theta = rT/c_s^2$ can be updated from any EOS without

any impact on the present demonstration. Note that classical EOS choices include athermal[1] $\theta = 1$, generalized athermal[25,26] $\theta = (\Delta x\,\mathrm{CFL})^2 / [\,(\Delta t(\mathrm{Ma}+1)c_s)^2\,\gamma]$ and ideal gas[22] $p = \rho c_s^2 \theta$. In these EOS we define $r = R/W$ with R the perfect gas constant, W the molecular weight and CFL the Courant-Friedrichs-Lewy number[27].

A. Reminders about Lattice-Boltzmann Method fundamentals

We first summarize the hybrid LB method. In this numerical method, physical information is projected onto n-th order Hermite polynomials $\mathcal{H}_i^{(n)}$ (see Appendix A) and stored on secondary variables f_i referred to as distributions. Each distribution f_i is associated to a discrete velocity c_i. The set of chosen velocities forms a lattice. Contrary to Navier-Stokes solvers, evolution equations for variables f_i are explicitly discretized rather than macroscopic conservation equations (e.g. mass, momentum, energy). Then, macroscopic quantities are obtained from distributions using Hermite $a^{f,(n)}_{\alpha_1\ldots\alpha_n}$ or raw moments $\Pi^{f,(n)}_{\alpha_1\ldots\alpha_n}$, defined as,

$$a^{f,(n)}_{\alpha_1\ldots\alpha_n} = \sum_i \mathcal{H}^{(n)}_{i\alpha_1\ldots\alpha_n} f_i\,, \qquad \Pi^{f,(n)}_{\alpha_1\ldots\alpha_n} = \sum_i c_{i\alpha_1}\ldots c_{i\alpha_n} f_i\,, \tag{1}$$

whose most important ones are mass and momentum

$$\rho = \sum_i f_i\,, \qquad \rho u_\alpha = \sum_i c_{i\alpha} f_i\,. \tag{2}$$

The LB scheme provides a numerical approximation to the discrete velocity Boltzmann equation,

$$\frac{\partial f_i}{\partial t} + c_{i\alpha}\frac{\partial f_i}{\partial x_\alpha} = -\frac{1}{\tau} f_i^{neq}\,, \tag{3}$$

where the right hand side was chosen as the classical single relaxation time τ model known as Bhatnagar-Gross-Krook (BGK) collision operator[28], $f_i^{neq} = f_i - f_i^{eq}$. A small scale expansion, e.g. the Chapman-Enskog expansion[1], shows that this discrete velocity Boltzmann equation (DVBE) provides very close approximations to NS solutions. However, looking for an efficient compressible LB solver, one often relies on narrow stencils, with usually only one layer of neighbours. Those stencils are called lattices, the most usual ones are D2Q9, D3Q19 and D3Q27, in which D stands for the spatial dimension and Q for the rank of the system, which is equal to the number of distributions f_i and discrete velocities $c_{i\alpha}$. Due to these standard lattices, velocity space is insufficiently discretized, and both an accurate energy conservation and stress tensor are missing, leading to the well known $O(\mathrm{Ma}^3)$ error[1], which is due to truncature errors in the velocity space.

On standard lattice one generally has $D^{f,(3)}_{\alpha\beta\gamma}$ an isotropy defect, defined by subtracting continuous and discrete moments

$$D^{f,(3)}_{\alpha\beta\gamma} = \int c_\alpha c_\beta c_\gamma f d\boldsymbol{c} - \Pi^{f,(3)}_{\alpha\beta\gamma} \neq 0\,. \tag{4}$$

The stress-tensor defect can be corrected by adding force terms[22,29–31] while the inaccurate energy conservation is restored by an *ad hoc* coupling with an energy equation solved by (e.g.) finite differences. This purely numerical coupling along with modeling of the collision kernel which is not taken into account by the Chapman-Enskog expansion leads to rely on more classical computational fluid dynamics tools such as the Taylor expansion and modified equation analysis[17,26], that show more accurately how LB solutions are related to NS ones. Nevertheless, LB algorithms provide close solutions to NS at low computational cost. This efficiency[32] comes from its simple collide and stream algorithm,

$$f_i^{col}(t,\boldsymbol{x}) = f_i^{eq}(t,\boldsymbol{x}) + \left(1 - \frac{\Delta t}{\overline{\tau}}\right)\overline{f}_i^{neq}(t,\boldsymbol{x}) + \frac{\Delta t}{2}F_i(t,\boldsymbol{x})\,, \tag{5}$$

$$\overline{f}_i(t+\Delta t,\boldsymbol{x}) = f_i^{col}(t,\boldsymbol{x} - \boldsymbol{c_i}\,\Delta t)\,, \tag{6}$$

where $\overline{\tau} = \tau + \Delta t/2$ The most important part of the algorithm that governs the physical modeling occurs is the equilibrium distribution f_i^{eq}. It is usually a function of macroscopic variables such as density ρ, momentum ρu_α and normalized temperature θ. In the case of regularized kernels, the non-equilibrium population $\overline{f}_i^{neq}$ is the second place where physical modeling occurs, it is usually reconstructed as a function of the equilibrium population f_i^{eq}, its macroscopic moments and gradients of those moments. Note that the usual and simplest choice is the BGK collision model, $\overline{f}_i^{neq} = \overline{f}_i - f_i^{eq} + \frac{\Delta t}{2}F_i$, where F_i is a numerical population including the effect of forces in mass and momentum equations through what is called a Guo forcing[1]. Lastly, f_i^{col} and $\overline{f}_i$ are the post-collision and post-streaming populations, respectively. Starting from a known solution at time t and using equations Eqs.(5,6), allows to obtain a post-collide streamed population. Then, taking raw moments of this population and updating together a second thermodynamic variable through finite differences (FD) provides the updated macroscopic solution at time $t + \Delta t$. This leads to a hybrid-LB scheme in which mass and momentum update arises from the LB scheme while the second thermodynamic variable is updated by the FD scheme.

B. Forceless pressure-based model

Full details of this model can be found in[13]. The numerical algorithm is summarized as follows. For regularized kernels, a restricted number of variables is sufficient to describe the system, therefore, the initial solution of the simulation is characterized by $[\rho, \rho u_\alpha, \theta, \Pi^{neq}_{\alpha\beta}](t, \boldsymbol{x})$. In order to get the updated solution $[\rho, \rho u_\alpha, \theta, \Pi^{neq}_{\alpha\beta}](t + \Delta t, \boldsymbol{x})$, several steps should be performed :

- The p-based equilibrium distribution $f_i^{p,eq}$ is reconstructed from $(t, \boldsymbol{x})$ moments

$$f_i^{p,eq}(t, \boldsymbol{x}) = \omega_i \left\{ \mathcal{H}^{(0)} \rho\theta + \frac{\mathcal{H}^{(1)}_{i\alpha}}{c_s^2} \rho u_\alpha + \frac{\mathcal{H}^{(2)}_{i\alpha\beta}}{2c_s^4} [\rho u_\alpha u_\beta] + \frac{\mathcal{H}^{(3)}_{i\alpha\beta\gamma}}{6c_s^6} [\rho u_\alpha u_\beta u_\gamma] \right\} (t, \boldsymbol{x}) \,. \tag{7}$$

- The non-equilibrium distribution $\overline{f}_i^{neq}(t, \boldsymbol{x})$ is also reconstructed from moments $\left[\rho, \rho u_\alpha, \Pi^{neq}_{\alpha\beta}\right](t, \boldsymbol{x})$ using either the projected[33] or recursive[34,35] regularization.

- Collision and streaming are performed,

$$f_i^{p,col}(t, \boldsymbol{x}) = f_i^{p,eq}(t, \boldsymbol{x}) + \left(1 - \frac{\Delta t}{\overline{\tau}}\right) \overline{f}_i^{neq}(t, \boldsymbol{x}) \,, \tag{8}$$

$$\overline{f}_i^{p}(t + \Delta t, \boldsymbol{x}) = f_i^{p,col}(t, \boldsymbol{x} - \boldsymbol{c_i}\, \Delta t) \,. \tag{9}$$

- Then the macroscopic reconstruction reads

$$\rho(t + \Delta t, \boldsymbol{x}) = \sum_i \overline{f}_i^{p}(t + \Delta t, \boldsymbol{x}) + \rho(t, \boldsymbol{x})[1 - \theta(t, \boldsymbol{x})]. \tag{10}$$

$$\rho u_\alpha(t + \Delta t, \boldsymbol{x}) = \sum_i c_{i\alpha} \overline{f}_i^{p}(t + \Delta t, \boldsymbol{x}) \,, \tag{11}$$

$$\Pi^{\overline{f}^{neq}}_{\alpha\beta}(t + \Delta t, \boldsymbol{x}) = \sum_i c_{i\alpha} c_{i\beta} \left[\overline{f}_i^{p} - f_i^{p,eq}\right] (t + \Delta t, \boldsymbol{x}) \,, \tag{12}$$

- To close the system, a finite difference scheme is used to update an additional thermodynamic variable such as entropy[13,22,24] or total energy[36]. From this additional step, $\theta(t + \Delta t, \boldsymbol{x})$ is now updated.

Then, one can apply recursively this algorithm from time $(t, \boldsymbol{x})$ to time $(t + \Delta t, \boldsymbol{x})$. This scheme therefore provides the regularized p-based numerical solution $\forall t = N_t\, \Delta t$ with $N_t \in \mathbb{N}$.

C. Forceless improved density-based model

In this model[21] a free parameter Θ was introduced. This parameter will be addressed later, but in the present section we consider the case $\Theta = 0$. Similarly to the p-based algorithm, the initial solution $[\rho, \rho u_\alpha, \theta, \Pi^{neq}_{\alpha\beta}](t, \boldsymbol{x})$ is known. In order to get the updated solution $(t + \Delta t, \boldsymbol{x})$ using the regularized improved ρ-based model, one should perform the following steps,

- Compute the equilibrium population,

$$f_i^{\rho,eq}(t, \boldsymbol{x}) = \omega_i \left\{ \mathcal{H}^{(0)} \rho + d_i + \frac{\mathcal{H}^{(1)}_{i\alpha}}{c_s^2} \rho u_\alpha + \frac{\mathcal{H}^{(2)}_{i\alpha\beta}}{2c_s^4} [\rho u_\alpha u_\beta] + \frac{\mathcal{H}^{(3)}_{i\alpha\beta\gamma}}{6c_s^6} [\rho u_\alpha u_\beta u_\gamma] \right\} (t, \boldsymbol{x}) \,, \quad (13)$$

  where d_i is defined as

$$d_i = \begin{cases} \rho[\theta - 1] & \text{if} \quad i \neq 0 \\ \dfrac{\omega_0 - 1}{\omega_0} \rho[\theta - 1] & \text{if} \quad i = 0 \end{cases} \quad (14)$$

  with ω_0 the lattice weight for the non-moving population $i = 0$.

- The non-equilibrium population $\overline{f}_i^{neq}$ is computed from a regularized collision kernel[33–35].

- Collision and streaming are performed

$$f_i^{\rho,col}(t, \boldsymbol{x}) = f_i^{\rho,eq}(t, \boldsymbol{x}) + \left(1 - \frac{\Delta t}{\overline{\tau}}\right) \overline{f}_i^{neq}(t, \boldsymbol{x}) \,, \quad (15)$$

$$\overline{f}_i^{\rho}(t + \Delta t, \boldsymbol{x}) = f_i^{\rho,col}(t, \boldsymbol{x} - \boldsymbol{c_i}\, \Delta t) \,. \quad (16)$$

- The macroscopic reconstruction reads

$$\rho(t + \Delta t, \boldsymbol{x}) = \sum_i \overline{f}_i^{\rho}(t + \Delta t, \boldsymbol{x}). \quad (17)$$

$$\rho u_\alpha(t + \Delta t, \boldsymbol{x}) = \sum_i c_{i\alpha} \overline{f}_i^{\rho}(t + \Delta t, \boldsymbol{x}) \,, \quad (18)$$

$$\Pi^{\overline{f}^{neq}}_{\alpha\beta}(t + \Delta t, \boldsymbol{x}) = \sum_i c_{i\alpha} c_{i\beta} \left[\overline{f}_i^{\rho} - f_i^{\rho,eq} \right] (t + \Delta t, \boldsymbol{x}) \,. \quad (19)$$

- Similarly to the p-based model, to close the system an additional thermodynamic variable is solved through a finite difference scheme, which is sufficient to get $\theta(t + \Delta t, \boldsymbol{x})$.

This algorithm can be used to update the numerical solution from $(t, \boldsymbol{x})$ to $(t + \Delta t, \boldsymbol{x})$. Applying this procedure recursively finally leads to the regularized improved ρ-based numerical solution $\forall t = N_t\, \Delta t$ with $N_t \in \mathbb{N}$.

D. Forceless model comparison

We now prove that it is possible to bridge between the p-based model (Section II B) and the improved ρ-based model (Section II C). Starting from the latter, we inject Eq.(14) inside Eq.(13), using the p-based equilibrium definition Eq.(7) leading to

$$f_i^{\rho,eq}(t,\boldsymbol{x}) = \begin{cases} f_i^{p,eq}(t,\boldsymbol{x}) \quad \text{if} \quad i \neq 0 \\ f_i^{p,eq}(t,\boldsymbol{x}) - \rho(t,\boldsymbol{x})[\theta(t,\boldsymbol{x}) - 1] \quad \text{if} \quad i = 0 \end{cases} \tag{20}$$

To allow for a fair comparison, we assume that i) both models start from the same initial solution and ii) the collision kernel is a function of the initial moments. Considering the initial solution $[\rho, \rho u_\alpha, \Pi^{neq}_{\alpha\beta}](t,\boldsymbol{x})$, this means that the reconstructed non-equilibrium term $\overline{f}_i^{neq}$ is identical between both models because it has been reconstructed from the same initial condition, with the same procedure. For example, the recursive regularization[35],

$$\overline{f}_i^{neq} = \omega_i \left\{ \frac{\mathcal{H}^{(2)}_{i\alpha\beta}}{2c_s^4} \Pi^{neq,(2)}_{\alpha\beta} + \frac{\mathcal{H}^{(3)}_{i\alpha\beta\gamma}}{6c_s^6} \left(u_\alpha \Pi^{neq,(2)}_{\beta\gamma} + u_\beta \Pi^{neq,(2)}_{\gamma\alpha} + u_\gamma \Pi^{neq,(2)}_{\alpha\beta} \right) \right\}, \tag{21}$$

could be used, which clearly shows that choosing the same initial solution $[\rho, \rho u_\alpha, \Pi^{neq}_{\alpha\beta}](t,\boldsymbol{x})$ trivially leads to $\overline{f}_i^{p,neq} = \overline{f}_i^{\rho,neq}$ in this case. Using both Eq.(20) and the equivalence between non-equilibrium populations allows us to write

$$f_i^{\rho,col} = \begin{cases} f_i^{p,col}(t,\boldsymbol{x}) \quad \text{if} \quad i \neq 0, \\ f_i^{p,col}(t,\boldsymbol{x}) - \rho(t,\boldsymbol{x})[\theta(t,\boldsymbol{x}) - 1] \quad \text{if} \quad i = 0, \end{cases} \tag{22}$$

This equation established a formal link between collided populations Eqs.(8,15). Now that collision was analyzed, the streaming step of both models can be linked using Eq.(16,22),

$$\overline{f}_i^{\rho}(t + \Delta t, \boldsymbol{x}) = \begin{cases} \overline{f}_i^{p}(t + \Delta t, \boldsymbol{x}) \quad \text{if} \quad i \neq 0 \\ \overline{f}_i^{p}(t + \Delta t, \boldsymbol{x}) - \rho(t,\boldsymbol{x})[\theta(t,\boldsymbol{x}) - 1] \quad \text{if} \quad i = 0 \end{cases} \tag{23}$$

Here, it is important noticing the temporal evaluation "t" of the $\rho[\theta - 1]$ term. This comes from the non-moving $i = 0$ population, which means that

$$\overline{f}_0^{\rho}(t + \Delta t, \boldsymbol{x}) = f_0^{\rho,col}(t,\boldsymbol{x}) = f_0^{p,col}(t,\boldsymbol{x}) - \rho(t,\boldsymbol{x})[\theta(t,\boldsymbol{x}) - 1] \tag{24}$$

Injecting Eq.(23) inside Eqs.(17-19) and using the fact that $c_{0\alpha} = 0$ leads to

$$\rho(t+\Delta t, \boldsymbol{x}) = \sum_i \overline{f}_i^p(t+\Delta t, \boldsymbol{x}) + \rho(t, \boldsymbol{x})[1-\theta(t, \boldsymbol{x})], \tag{25}$$

$$\rho u_\alpha(t+\Delta t, \boldsymbol{x}) = \sum_i c_{i\alpha}\overline{f}_i^p(t+\Delta t, \boldsymbol{x}), \tag{26}$$

$$\Pi_{\alpha\beta}^{\overline{f}^{neq}}(t+\Delta t, \boldsymbol{x}) = \sum_i c_{i\alpha}c_{i\beta}\left[\overline{f}_i^p - f_i^{p,eq}\right](t+\Delta t, \boldsymbol{x}). \tag{27}$$

Which is exactly identical to Eqs.(10-12). Therefore, from the initial solution $[\rho, \rho u_\alpha, \Pi_{\alpha\beta}^{neq}](t, \boldsymbol{x})$, both the p-based and the improved ρ-based lead to the same updated solution $[\rho, \rho u_\alpha, \Pi_{\alpha\beta}^{neq}](t+\Delta t, \boldsymbol{x})$. In other words, the hybrid recursive regularized p-based model[13] and improved ρ-based model[21] are strictly equivalent in the absence of force terms and other coupled physical models. More details on the equivalence between both models can be found in Appendix B where we highlight how a similar bridge can also be obtained for BGK collision kernel.

E. Comparison accounting for force terms

Having demonstrated the equivalence in the absence of force corrective terms in the previous section, it is natural to infer that the force terms of both models should be equivalent up to negligible errors. We denote the corrective force term associated with p-based or improved ρ-based models by $F_i^{p,\rho}$. From[13] and[21] we find that,

$$F_i^{p,\rho} = \omega_i \frac{\mathcal{H}_{i\alpha\beta}^{(2)}}{2c_s^4}\left[a_{\alpha\beta}^C + a_{\alpha\beta}^{p,\rho}\right], \tag{28}$$

where $a_{\alpha\beta}^C$ is the lattice dependent component of the force term shared by both models,

$$a_{\alpha\beta}^C = c_s^2\left[u_\alpha\frac{\partial\rho(1-\theta)}{\partial x_\beta} + u_\beta\frac{\partial\rho(1-\theta)}{\partial x_\alpha}\right] - \frac{\partial D_{\alpha\beta\gamma}^{f^{eq},(3)}}{\partial x_\gamma}, \tag{29}$$

For the D3Q19r basis (see Appendix A) which is the lattice used in this study,

$$\frac{\partial D_{\alpha\beta\gamma}^{f^{eq},(3)}}{\partial x_\gamma} = \delta_{\alpha\beta}\frac{\partial\rho u_\alpha^3}{\partial x_\alpha} + (1-\delta_{\alpha\beta})\frac{\partial\rho u_x u_y u_z}{\partial x_\psi}, \tag{30}$$

without summation over repeated index α and with ψ defined by $\psi \neq \alpha$ and $\psi \neq \beta$. Additionally, $a_{\alpha\beta}^{p,\rho}$ depends on the considered model,

$$a^{p}_{\alpha\beta} = \delta_{\alpha\beta}c_s^2\left(\frac{\partial\rho(\theta-1)}{\partial t} + \rho\frac{2}{D}\frac{\partial u_\gamma}{\partial x_\gamma}\right), \tag{31}$$

$$a^{\rho}_{\alpha\beta} = \delta_{\alpha\beta}c_s^2\left(u_\gamma\frac{\partial\rho(1-\theta)}{\partial x_\gamma} + \rho(1-\theta)\frac{D+2}{D}\frac{\partial u_\gamma}{\partial x_\gamma}\right). \tag{32}$$

A Taylor expansion of the lattice Boltzmann scheme[17] shows that in p-based and improved ρ-based the stress tensor equation reads

$$\begin{aligned} -\Pi^{f^{neq},(2)}_{\alpha\beta} &= \tau\rho c_s^2\left[\frac{\partial u_\alpha}{\partial x_\beta} + \frac{\partial u_\beta}{\partial x_\alpha}\right] + \tau\delta_{\alpha\beta}c_s^2\left[\frac{\partial\rho u_\gamma}{\partial x_\gamma} + \frac{\partial\rho\theta}{\partial t}\right] - \tau a^{p,\rho}_{\alpha\beta} \\ &+ \tau\Big[\frac{\partial\Pi^{f^{neq},(2)}_{\alpha\beta}}{\partial t} + \frac{\partial\left[\Pi^{f^{neq},(3)}_{\alpha\beta\gamma} - D^{f^{neq},(3)}_{\alpha\beta\gamma}\right]}{\partial x_\gamma}\Big] - \tau\Big[u_\alpha\frac{\partial\Pi^{f^{neq},(2)}_{\beta\gamma}}{\partial x_\gamma} + u_\beta\frac{\partial\Pi^{f^{neq},(2)}_{\alpha\gamma}}{\partial x_\gamma}\Big]. \end{aligned} \tag{33}$$

Note that in the case of the recursive regularized kernel, $\Pi^{f^{neq},(3)}_{\alpha\beta\gamma}$ being a linear function of $\Pi^{f^{neq},(2)}_{\alpha\beta}$, injecting Eq.(33) into itself similarly to[24,26] leads to the more tractable equation,

$$-\Pi^{f^{neq},(2)}_{\alpha\beta} = \tau\rho c_s^2\left[\frac{\partial u_\alpha}{\partial x_\beta} + \frac{\partial u_\beta}{\partial x_\alpha}\right] + \tau\delta_{\alpha\beta}c_s^2\left[\frac{\partial\rho u_\gamma}{\partial x_\gamma} + \frac{\partial\rho\theta}{\partial t}\right] - \tau a^{p,\rho}_{\alpha\beta} + O(\tau^2). \tag{34}$$

In order to further analyze the improved ρ-based, it is necessary to express the time derivative $\frac{\partial\rho\theta}{\partial t}$. Considering a perfect gas equation of state $p = \rho\theta c_s^2$ and combining the mass, momentum and total energy equations one gets the following pressure equation,

$$\frac{1}{\gamma-1}\Big(\frac{\partial\rho\theta}{\partial t} + \frac{\partial\rho\theta u_\beta}{\partial x_\beta}\Big) + \rho\theta\frac{\partial u_\gamma}{\partial x_\gamma} - \frac{\partial}{\partial x_\gamma}\left(\lambda\frac{\partial\theta}{\partial x_\gamma}\right) + c_s^{-2}\Pi^{f^{neq},(2)}_{\beta\gamma}\frac{\partial u_\beta}{\partial x_\gamma} = 0. \tag{35}$$

Assuming a Prandtl number $\mathrm{Pr} \geq O(1)$, it is reasonable to rewrite Eq.(35) as

$$\frac{\partial\rho\theta}{\partial t} + \frac{\partial\rho\theta u_\beta}{\partial x_\beta} + \rho\theta(\gamma-1)\frac{\partial u_\gamma}{\partial x_\gamma} = O(\tau). \tag{36}$$

Using Eqs.(32,34,36) leads to the improved ρ-based stress tensor

$$-\Pi^{f^{neq},(2)}_{\alpha\beta} = \tau\rho c_s^2\left[\frac{\partial u_\alpha}{\partial x_\beta} + \frac{\partial u_\beta}{\partial x_\alpha} - \delta_{\alpha\beta}\frac{2}{D}\frac{\partial u_\gamma}{\partial x_\gamma}\right] + \tau\delta_{\alpha\beta}c_s^2\rho\theta\left[\frac{D+2}{D} - \gamma\right]\frac{\partial u_\gamma}{\partial x_\gamma} + O(\tau^2), \tag{37}$$

in which an uncontrolled bulk viscosity appears, similarly to what was pointed out in[24]. Note that due to the second law of thermodynamics a positive bulk viscosity $\left(\frac{D+2}{D} - \gamma\right) \geq 0$ is mandatory[37]. In both the initial ρ-based model[22] and the improved ρ-based model[21], bulk viscosity is nonzero.

This is due to the mismatch between the actual adiabatic exponent γ of the simulation and the natural adiabatic exponent $\gamma_{LB} = \frac{D+2}{D}$ arising from the chosen D dimensional lattice. Inspired by[24], one can easily get rid of this uncontrolled bulk by replacing Eq.(32) by

$$\tilde{a}^{\rho}_{\alpha\beta} = \delta_{\alpha\beta} c_s^2 \left(u_\gamma \frac{\partial \rho(1-\theta)}{\partial x_\gamma} + \rho \left[\frac{D+2}{D} - \gamma\theta \right] \frac{\partial u_\gamma}{\partial x_\gamma} \right) . \tag{38}$$

In this case the stress tensor obtained from the improved ρ-based with zero bulk viscosity defined by Eqs.(34,38) is now equivalent up to a different $O(\tau^2)$ error to the p-based one given by Eqs.(31,34),

$$-\Pi^{f^{neq},(2)}_{\alpha\beta} = \tau \rho c_s^2 \left[\frac{\partial u_\alpha}{\partial x_\beta} + \frac{\partial u_\beta}{\partial x_\alpha} - \delta_{\alpha\beta} \frac{2}{D} \frac{\partial u_\gamma}{\partial x_\gamma} \right] + O(\tau^2) . \tag{39}$$

This is due to the fact that $a^{p}_{\alpha\beta} = \tilde{a}^{\rho}_{\alpha\beta} + O(\tau)$, leading to a $O(\tau^2)$ difference between the p-based stress tensor Eq.(39) and the zero-bulk viscosity improved ρ-based stress tensor obtained from Eqs.(34,38). This shows that when the corrective force term is taken into account, models[13,21] become rigorously different, yet a strong connection still exists between them.

III. UNIFIED MODEL ON STANDARD LATTICE

In this section, we propose to build a numerical LB scheme meant to unify preexisting compressible models discussed above[13,22–24]. For the sake of completeness, additional mass source $\dot{m}$, momentum force $\rho\mathcal{F}_\alpha$ and energy source $\rho\dot{q}$ are included. The LB scheme first provides mass and momentum conservations,

$$\frac{\partial \rho}{\partial t} + \frac{\partial \rho u_\beta}{\partial x_\beta} = \dot{m} \tag{40}$$

$$\frac{\partial \rho u_\alpha}{\partial t} + \frac{\partial \left[\rho u_\alpha u_\beta + p\delta_{\alpha\beta} + \Pi^{neq}_{\alpha\beta} \right]}{\partial x_\beta} = \rho \mathcal{F}_\alpha . \tag{41}$$

completed by a second thermodynamic variable solved by FD. Usual choices are among the total energy, internal energy and entropy equations,

$$\frac{\partial \rho E}{\partial t} + \frac{\partial (\rho E + p) u_\beta + q_\beta - u_\alpha \Pi^{neq}_{\alpha\beta}}{\partial x_\beta} = \rho \mathcal{F}_\alpha u_\gamma + \rho\dot{q} , \tag{42}$$

$$\frac{\partial \rho e}{\partial t} + \frac{\partial \rho e u_\beta}{\partial x_\beta} + p \frac{\partial u_\gamma}{\partial x_\gamma} + \frac{\partial q_\gamma}{\partial x_\gamma} - \Pi^{neq}_{\alpha\beta} \frac{\partial u_\beta}{\partial x_\gamma} = \rho\dot{q} + \dot{m} \frac{u_\gamma^2}{2} , \tag{43}$$

$$\rho T \left(\frac{\partial s}{\partial t} + u_\beta \frac{\partial s}{\partial x_\beta} \right) + \frac{\partial q_\gamma}{\partial x_\gamma} - \Pi^{neq}_{\alpha\beta} \frac{\partial u_\beta}{\partial x_\gamma} = \rho\dot{q} + \dot{m} \left(\frac{u_\gamma^2}{2} - e - \frac{p}{\rho} \right) . \tag{44}$$

Hydrodynamic equations (40,41) are coupled to thermal effects Eqs.(42,43,44) through the perfect gas EOS $p = \rho r T$, $e = C_v T$ and heat capacities $C_v = r/(\gamma-1)$ and $C_p = \gamma r/(\gamma-1)$. Then, combining Eqs.(40,41) with any choice among Eqs.(42,43,44) and assuming a constant r and γ values one gets the kinetic tensor and pressure equations,

$$\frac{\partial \rho u_\alpha u_\beta}{\partial t} + \frac{\partial \rho u_\alpha u_\beta u_\gamma}{\partial x_\gamma} + u_\alpha \frac{\partial p}{\partial x_\beta} + u_\beta \frac{\partial p}{\partial x_\alpha} + O(\tau) = \rho \mathcal{F}_\alpha u_\beta + \rho \mathcal{F}_\beta u_\alpha - \dot{m} u_\alpha u_\beta \,, \tag{45}$$

$$\frac{1}{\gamma - 1}\left(\frac{\partial p}{\partial t} + \frac{\partial p u_\beta}{\partial x_\beta}\right) + p \frac{\partial u_\gamma}{\partial x_\gamma} + O(\tau) = \rho \dot{q} + \dot{m} \frac{u_\gamma^2}{2} \,, \tag{46}$$

written in a compact form in which $O(\tau)$ accounts for viscous and heat conductive terms. Then, Eqs.(40-44) are closed by computing the heat flux q_α through FD,

$$q_\alpha = -\lambda \frac{\partial T}{\partial x_\alpha} \,, \tag{47}$$

and by using a proper correction term during collision so that LB stress tensor is

$$-\Pi_{\alpha\beta}^{f^{neq},(2)} = \mu \left[\frac{\partial u_\alpha}{\partial x_\beta} + \frac{\partial u_\beta}{\partial x_\alpha} - \delta_{\alpha\beta} \frac{2}{D} \frac{\partial u_\gamma}{\partial x_\gamma}\right] + O(\tau^2) \,. \tag{48}$$

A. Unified LB scheme

Now, we provide detailed equations of the unified model. For the sake of clarity, we use the improved ρ-based format. The unified equilibrium distribution f_i^{eq} is

$$\begin{aligned} f_i^{eq} = \omega_i \Big\{ & \rho + \frac{\omega_i - \delta_{0i}}{\omega_i} \rho [\theta - 1](1 - \zeta) + \frac{\mathcal{H}_{i\alpha}^{(1)}}{c_s^2} \rho u_\alpha + \frac{\mathcal{H}_{i\alpha\beta}^{(2)}}{2c_s^4} \left[\rho u_\alpha u_\beta + \zeta \delta_{\alpha\beta} \rho c_s^2 (\theta - 1)\right] \\ & + \frac{\mathcal{H}_{i\alpha\beta\gamma}^{(3)}}{6c_s^6} \left[\rho u_\alpha u_\beta u_\gamma - \kappa \rho c_s^2 \left(u_\alpha \delta_{\beta\gamma} + u_\beta \delta_{\gamma\alpha} + u_\gamma \delta_{\alpha\beta}\right)\right] \Big\} \,, \end{aligned} \tag{49}$$

in which two arbitrary fields $\zeta(t, \boldsymbol{x})$ and $\kappa(t, \boldsymbol{x})$ have been introduced. A Taylor expansion[17] shows that a force term is necessary to account for mass $\dot{m}$, momentum $\rho \mathcal{F}_\alpha$ and energy $\rho \dot{q}$ sources. Another force term is also necessary to remove significant errors in the stress tensor introduced by isotropy defects Eq.(4). Complete forcing terms can follow two different strategies F_i and G_i, they are equivalent up to a $O(\tau)$ difference and read as

$$F_i = \omega_i \left\{ \mathcal{H}^{(0)} \dot{m} + \frac{\mathcal{H}_{i\alpha}^{(1)}}{c_s^2} \rho \mathcal{F}_\alpha + \frac{\mathcal{H}_{i\alpha\beta}^{(2)}}{2c_s^4} a_{\alpha\beta}^{F,(2)} \right\} \,, \tag{50}$$

$$G_i = \omega_i \left\{ \mathcal{H}^{(0)} \dot{m} + \frac{\mathcal{H}_{i\alpha}^{(1)}}{c_s^2} \rho \mathcal{F}_\alpha + \frac{\mathcal{H}_{i\alpha\beta}^{(2)}}{2c_s^4} a_{\alpha\beta}^{G,(2)} \right\} \,, \tag{51}$$

in which Hermite moments $a_{\alpha\beta}^{F,(2)}$ and $a_{\alpha\beta}^{G,(2)}$ are

$$a_{\alpha\beta}^{F,(2)} = \frac{2}{D}\delta_{\alpha\beta}(1-\kappa)\rho c_s^2\frac{\partial u_\gamma}{\partial x_\gamma} - \delta_{\alpha\beta}c_s^2\frac{\partial\rho(1-\theta)}{\partial t} - \delta_{\alpha\beta}c_s^2\frac{\partial\rho\kappa u_\gamma}{\partial x_\gamma} + a_{\alpha\beta}^C + \rho\mathcal{F}_\alpha u_\beta + \rho\mathcal{F}_\beta u_\alpha - \dot{m}u_\alpha u_\beta\,, \tag{52}$$

$$a_{\alpha\beta}^{G,(2)} = \delta_{\alpha\beta}c_s^2\rho\left(\frac{2}{D}(1-\kappa) - (\gamma-1)\,\theta\right)\frac{\partial u_\gamma}{\partial x_\gamma} + \delta_{\alpha\beta}c_s^2\frac{\partial\rho(1-\theta-\kappa)u_\gamma}{\partial x_\gamma} - \dot{m}\left(\delta_{\alpha\beta}c_s^2 + u_\alpha u_\beta - \frac{(\gamma-1)\,u_\gamma^2}{2}\delta_{\alpha\beta}\right) + \delta_{\alpha\beta}\,(\gamma-1)\,\rho\dot{q} + a_{\alpha\beta}^C + \rho\mathcal{F}_\alpha u_\beta + \rho\mathcal{F}_\beta u_\alpha\,, \tag{53}$$

where $a_{\alpha\beta}^C$ is the lattice-dependent component of the force term,

$$a_{\alpha\beta}^C = c_s^2\left[u_\alpha\frac{\partial\rho(1-\theta-\kappa)}{\partial x_\beta} + u_\beta\frac{\partial\rho(1-\theta-\kappa)}{\partial x_\alpha}\right] - \frac{\partial D_{\alpha\beta\gamma}^{f^{eq},(3)}}{\partial x_\gamma}\,, \tag{54}$$

For the D3Q19r basis (see Appendix A) which is the chosen basis in this study,

$$-\frac{\partial D_{\alpha\beta\gamma}^{f^{eq},(3)}}{\partial x_\gamma} = \delta_{\alpha\beta}\frac{\partial\rho u_\alpha(\kappa-u_\alpha^2)}{\partial x_\alpha} - (1-\delta_{\alpha\beta})\frac{\partial\rho u_x u_y u_z}{\partial x_\psi}\,, \tag{55}$$

in which no summation over repeated index α is done and ψ is chosen as $\psi\neq\alpha$ and $\psi\neq\beta$. It is worth noting that $a_{\alpha\beta}^{F,(2)}$ and $a_{\alpha\beta}^{G,(2)}$ can be considered as generalizations of force term strategies respectively employed in[13] and[21,24]. Using either F_i or G_i in the usual collide, stream and macroscopic reconstruction procedure then leads to a unified LB numerical scheme which is consistent with Eqs.(40,41), completed by a stress tensor equation,

$$-\Pi_{\alpha\beta}^{f^{neq},(2)} = \tau(1-\kappa)\rho c_s^2\left[\frac{\partial u_\alpha}{\partial x_\beta} + \frac{\partial u_\beta}{\partial x_\alpha} - \delta_{\alpha\beta}\frac{2}{D}\frac{\partial u_\gamma}{\partial x_\gamma}\right] + O(\tau^2)\ . \tag{56}$$

Identification procedure then states that $\mu=\tau(1-\kappa)\rho c_s^2$. Using equilibrium Eq.(49), force term Eq.(51), $\zeta=1$ and $\kappa=1-\theta$, this model recovers the zero-bulk viscosity ρ-based model[24]. With Eq.(50), $\zeta=0$ and $\kappa=0$, the p-based model[13] is recovered. Lastly, if Eq.(51) is used along with $\zeta=\frac{\Theta}{1-\theta}$ and $\kappa=\Theta$, the zero-bulk viscosity version of the improved ρ-based model is recovered, where Θ is a free parameter introduced in[21]. Through numerical experiments, the influence of the value proposed by[21] for Θ is found negligible, $\zeta=0$ and $\kappa=0$ are therefore chosen in this study to keep the model as simple as possible. In what follows it was chosen to use F_i instead of G_i. While it still unclear which one of the two corrections is the best one in term of accuracy and stability, there exists some compelling arguments to use F_i. First, because the Prandtl number is implicitly

contained in the pressure time derivative in F_i, this force term allows to handle arbitrary values or Pr while the force term G_i, by using Eq.(35) is restricted to $\mathrm{Pr} \geq O(1)$. Second, by avoiding the use of Eq.(35) to assess the consistency of the LB stress-tensor, F_i allows an easier coupling with complex EOS such as the van der Waals equation[38] or Noble Able stiffened gas[39]. Indeed, these EOS would lead to a more complicated pressure equation than Eq.(35) in which additional non dimensional numbers introduced by those EOS would also appear in consistency errors of the stress-tensor. Lastly, F_i does not involve using the heat release term $\dot{q}$, it is therefore easier to use in combustion applications. Force terms F_i and G_i are equivalent ($F_i = G_i + O(\tau)$) for monospecies fluids with order unity Pr which is our case here, but F_i is still shorter to implement, therefore it was retained in what follows.

B. Interpretation of δ_{0i}

Before moving to the algorithmic description of our scheme, we provide a simple explanation of how the classical ρ-based model[22–24] differs from recent models such as p-based[13] and improved ρ-based[21] in which the unusual Kronecker δ_{0i} is used, see Eq.(49) with $\zeta \neq 1$. Let's project δ_{0i} onto the D3Q19r Hermite basis (Appendix A),

$$a^{\delta_{0i},(0)} = \sum_i \mathcal{H}_i^{(0)} \delta_{0i} = 1\,, \tag{57}$$

$$a_\alpha^{\delta_{0i},(1)} = \sum_i \mathcal{H}_{i\alpha}^{(1)} \delta_{0i} = 0\,, \tag{58}$$

$$a_{\alpha\beta}^{\delta_{0i},(2)} = \sum_i \mathcal{H}_{i\alpha\beta}^{(2)} \delta_{0i} = -c_s^2 \delta_{\alpha\beta}\,, \tag{59}$$

$$a_{\alpha\beta\gamma}^{\delta_{0i},(3)} = \sum_i \mathcal{H}_{i\alpha\beta\gamma}^{(3)} \delta_{0i} = 0\,, \tag{60}$$

$$a^{\delta_{0i},\mathcal{A}_i} = \sum_i \mathcal{A}_i \delta_{0i} = 2c_s^4\,, \tag{61}$$

$$a^{\delta_{0i},\mathcal{B}_i} = \sum_i \mathcal{B}_i \delta_{0i} = 2c_s^4\,, \tag{62}$$

$$a^{\delta_{0i},C_i} = \sum_i C_i \delta_{0i} = 2c_s^4\,. \tag{63}$$

Then, we can exactly express δ_{0i} by

$$\delta_{0i} = \omega_i \left\{ \mathcal{H}_i^{(0)} - \frac{\mathcal{H}_{ixx}^{(2)} + \mathcal{H}_{iyy}^{(2)} + \mathcal{H}_{izz}^{(2)}}{2c_s^2} + \frac{\mathcal{A}_i + \mathcal{B}_i + C_i}{12c_s^4} \right\}. \tag{64}$$

Injecting Eq.(64) into Eq.(49) allows to write

$$f_i^{eq} = \omega_i \Big\{ \mathcal{H}^{(0)}\rho + \frac{\mathcal{H}^{(1)}_{i\alpha}}{c_s^2}\rho u_\alpha + \frac{\mathcal{H}^{(2)}_{i\alpha\beta}}{2c_s^4}\left[\rho u_\alpha u_\beta + \delta_{\alpha\beta}\rho c_s^2(\theta-1)\right] + \frac{\mathcal{H}^{(3)}_{i\alpha\beta\gamma}}{6c_s^6}\Big[\rho u_\alpha u_\beta u_\gamma - \kappa\rho c_s^2\left(u_\alpha\delta_{\beta\gamma} + u_\beta\delta_{\gamma\alpha} + u_\gamma\delta_{\alpha\beta}\right)\Big] - \frac{\mathcal{A}_i + \mathcal{B}_i + C_i}{12c_s^4}\rho[\theta-1](1-\zeta)\Big\}. \tag{65}$$

In other words, recent models such as p-based and improved ρ-based are equivalent to the classical ρ-based model[22–24] with additional information projected onto fourth order polynomials $\mathcal{A}_i$, $\mathcal{B}_i$ and C_i due to $\zeta \neq 1$ in Eq.(49). This is expected to change numerical errors of the LB scheme without changing the consistency of mass and momentum conservation equations.

C. Coupled models

The lattice Boltzmann scheme being now unified, this section aims at further comparing and unifying the different ingredients that were previously used in the compressible hybrid recursive regularized literature[13,22–24]. In this study, the chosen basis for simulations is the D3Q19r rotated symmetry basis[35], also used in[13,21,23], whose details can be found in Appendix A.

1. Thermal coupling

While Eqs.(42,43,44) are equivalent, their discretized counterparts may lead to highly different stability and accuracy properties. The entropy equation in non-conservative format being mainly an advection equation with source terms, it is easily discretized and leads to robust results, explaining this choice of energy variable, widely present in the LB literature[13,22–24]. Which is why in this study, an entropy equation solved by finite differences is chosen,

$$\frac{\partial s}{\partial t} + u_\beta\frac{\partial s}{\partial x_\beta} = \frac{1}{\rho T}\left[\Pi_{\alpha\beta}\frac{\partial u_\alpha}{\partial x_\beta} + \frac{\partial}{\partial x_\beta}\left(\lambda\frac{\partial T}{\partial x_\beta}\right)\right]. \tag{66}$$

In all previous studies, viscous heat and heat conduction were discretized by classical second order centered finite difference schemes while different strategies were employed for the convective term. When applied to a 1D passive scalar equation these advection schemes correspond to :

- In[22], a $O(\Delta t^2)$ accurate Runge-Kutta temporal integration is adopted along with a $O(\Delta x^3)$ accurate MUSCL scheme[40] resulting in a 9 points stencil between timesteps t and $t + \Delta t$.

- In[23,24], the stencil was simplified by replacing the Runge-Kutta 2 integration by a simpler $O(\Delta t)$ accurate Euler temporal integration. The spatial integration remained identical and the overall scheme leads to a 5 points stencil.

- In[13], time and space were discretized simultaneously by a MUSCL-Hancock[41] method, resulting in a compact $O(\Delta t^3, \Delta x^3)$ accurate 5 points stencil.

Due to its compactness and its high order of accuracy, the MUSCL-Hancock method is chosen for this study, the only difference being that the flux limiter was removed compared to[13]. Except the convective term, other terms are still discretized by second order centered schemes. Implementation details for MUSCL-Hancock and all numerical gradients used in this study can be found in Appendix C.

2. Non-equilibrium reconstruction

In this study, we follow the hybrid recursive regularized method along with the traceless non-equilibrium reconstruction[13,17], which has been identified[26] as a supplementary regularization for moment $\Pi_{\gamma\gamma}$. The non-equilibrium second order moment is then calculated using

$$\begin{aligned}\overline{\Pi}^{\mathrm{neq},(2)}_{\alpha\beta}(t,\boldsymbol{x}) = \sigma \sum_i \left[c_{i\alpha}c_{i\beta} - \frac{\delta_{\alpha\beta}}{3}c_{i\gamma}c_{i\gamma}\right]\left(\overline{f}_i(t,\boldsymbol{x}) - f_i^{\mathrm{eq}}(t,\boldsymbol{x}) + \frac{\Delta t}{2}F_i(t-\Delta t,\boldsymbol{x})\right) \\ - \left[(1-\sigma)(1-\kappa)\rho c_s^2\overline{\tau}\left(\frac{\partial u_\alpha}{\partial x_\beta} + \frac{\partial u_\beta}{\partial x_\alpha} - \frac{2\delta_{\alpha\beta}}{D}\frac{\partial u_\gamma}{\partial x_\gamma}\right)\right](t,\boldsymbol{x}) \end{aligned} \tag{67}$$

Where σ is the weighting free parameter introduced by[35]. Note the $t-\Delta t$ evaluation of F_i. Numerical experiments showed better stability properties for Ma $\gtrapprox$ 1.7 simulations than with the usual t evaluation, however, no measurable difference was observed for lower Ma numbers when using t. This change formally introduces a $O(\Delta t)$ error in the stress tensor, which is of the order of the leading numerical error already introduced by the non-BGK collision kernel[17,26,42]. Using, Eq.(67), the recursive regularized procedure states that

$$\overline{\Pi}^{\mathrm{neq},(3)}_{\alpha\beta\gamma}(t,\boldsymbol{x}) = \left[u_\alpha\overline{\Pi}^{\mathrm{neq},(2)}_{\beta\gamma} + u_\beta\overline{\Pi}^{\mathrm{neq},(2)}_{\gamma\alpha} + u_\gamma\overline{\Pi}^{\mathrm{neq},(2)}_{\alpha\beta}\right](t,\boldsymbol{x})\,. \tag{68}$$

Then, the recursive regularization with D3Q19r lattice (Appendix A) dictates that non-equilibrium should be defined as

$$\overline{f}_i^{\mathrm{neq}} = \omega_i\left\{\frac{\mathcal{H}^{(2)}_{i\alpha\beta}}{2c_s^4}\overline{\Pi}^{\mathrm{neq},(2)}_{\alpha\beta} + \frac{\mathcal{H}^{(3r)}_{i\alpha\beta\gamma}}{6c_s^6}\overline{\Pi}^{\mathrm{neq},(3r)}_{\alpha\beta\gamma}\right\}. \tag{69}$$

3. *Sensor, artificial bulk viscosity*

Through numerical experiments, we found that the excellent stability properties reported in[21] are largely due to an extra bulk viscosity μ_β added by the filtering process $|\Pi^{neq}_{\alpha\alpha}|= \min\left(0.1|\nabla\cdot u|, |\Pi^{neq}_{\alpha\alpha}|\right)$. This filtering process is found to sometimes create spurious acoustic noise near curved discontinuities. Therefore, a smoother artificial bulk viscosity $\mu_\beta = 0.05\,\mu\,\mathrm{Ma}$ is introduced in this study. Defining Ma as the local Mach number allows to write,

$$F_i^{\mu_\beta} = \omega_i \frac{\mathcal{H}^{(2)}_{i\alpha\beta}}{2c_s^4}\delta_{\alpha\beta}\rho c_s^2(\kappa-1)0.05\mathrm{Ma}\frac{\partial u_\gamma}{\partial x_\gamma}, \tag{70}$$

which is added only during collision, resulting in an additional first order forcing implementation. This bulk viscosity is meant to dump unstable acoustic modes in very high Mach number simulations. It is worth mentioning that this artificial bulk is only added in the lattice Boltzmann part of the algorithm and that the stability of all simulations that will be presented in this article does not depend on it, except for $\mathrm{Ma} \gtrapprox 1.7$. Nevertheless, Eq.(70) is kept in all test cases performed in this article. Additionally, to handle discontinuities, a sensor consisting of a normalized numerical Laplacian operator is used to define an artificial kinematic viscosity,

$$\nu_{sc} = s_c \left|\frac{\rho(x-\Delta x) - 2\rho(x) + \rho(x+\Delta x)}{\rho(x-\Delta x) + 2\rho(x) + \rho(x+\Delta x)}\right|, \tag{71}$$

where s_c is a free parameter. Then, this artificial viscosity is added to the physical dynamic viscosity, $\mu = \mu_{ph} + \rho\nu_{sc}$. Through numerical experiments, we found that contact discontinuities create as much or more Gibbs oscillations than shocks, explaining the unusual choice to evaluate Eq.(71) using ρ instead of p. This allows our sensor to be triggered by both shocks and contact discontinuities.

D. Step-by-step unified scheme

All necessary ingredients have been discussed, we shall now detail the step-by-step algorithm to get the updated solution $[\rho, \rho u_\alpha, \theta, \Pi^{neq}_{\alpha\beta}](t+\Delta t, \boldsymbol{x})$ from the last timestep solution $[\rho, \rho u_\alpha, \theta, \Pi^{neq}_{\alpha\beta}](t, \boldsymbol{x})$. We remind that for numerical simulations in this study, $\zeta = 0$ and $\kappa = 0$ have been retained along with force term F_i.

i) Knowing $[\rho, \rho u_\alpha, \theta, \Pi^{neq}_{\alpha\beta}](t, \boldsymbol{x})$, use the equation of state $s = C_v \ln c_s^2\theta\rho^{1-\gamma}$ to get the entropy $s(t, \boldsymbol{x})$as a function of $\rho(t, \boldsymbol{x})$ and $\theta(t, \boldsymbol{x})$.

ii) Compute the equilibrium distribution $f_i^{eq}(t,\boldsymbol{x})$ using Eq.(49) and the rotated D3Q19r basis (Appendix A).

iii) Compute either $F_i(t,\boldsymbol{x})$ and $F_i^{\mu_\beta}(t,\boldsymbol{x})$ using Eqs.(50,70).

iv) Compute the non-equilibrium $\overline{f}_i^{neq}(t,\boldsymbol{x})$ using Eqs.(68-69).

v) Compute the collided population $f_i^{col}(t,\boldsymbol{x})$ as

$$f_i^{col}(t,\boldsymbol{x}) = f_i^{eq}(t,\boldsymbol{x}) + \left(1 - \frac{\Delta t}{\overline{\tau}}\right)\overline{f}_i^{neq}(t,\boldsymbol{x}) + \Delta t\left(\frac{1}{2}F_i + F_i^{\mu_\beta}\right)(t,\boldsymbol{x})\,. \tag{72}$$

vi) Shift the populations along lattices following the streaming,

$$\overline{f}_i(t+\Delta t,\boldsymbol{x}) = f_i^{col}(t,\boldsymbol{x} - \boldsymbol{c_i}\,\Delta t)\,. \tag{73}$$

vii) Equilibrium moments can now be updated as

$$\rho(t+\Delta t,\boldsymbol{x}) = \sum_i \overline{f}_i(t+\Delta t,\boldsymbol{x}) + \frac{\Delta t}{2}\dot{m}(t+\Delta t,\boldsymbol{x})\,, \tag{74}$$

$$\rho u_\alpha(t+\Delta t,\boldsymbol{x}) = \sum_i c_{i\alpha}\overline{f}_i(t+\Delta t,\boldsymbol{x}) + \frac{\Delta t}{2}[\rho\mathcal{F}_\alpha](t+\Delta t,\boldsymbol{x})\,, \tag{75}$$

viii) Solve the entropy equation following numerical schemes presented in Appendix C in order to get the updated $s(t+\Delta t,\boldsymbol{x})$ and use it along with $\rho(t+\Delta t,\boldsymbol{x})$ to get the updated normalized temperature $\theta(t+\Delta t,\boldsymbol{x})$ through $\theta = c_s^{-2}\rho^{\gamma-1}e^{s/C_v}$.

ix) Then, the updated stress tensor can be computed from Eqs.(49-50,67).

After those steps, $[\rho, \rho u_\alpha, \theta, \Pi_{\alpha\beta}^{neq}](t+\Delta t,\boldsymbol{x})$ is now updated.

IV. NUMERICAL VALIDATIONS

A. Isentropic vortex

An isentropic vortex initialized in a 2D fully periodic box of size $[10\times 10]$ and discretized by a 200×200 mesh is simulated. This unity radius vortex $R=1$ is transported over a distance $200R$ corresponding to 20 flow through time periods. The Ma number of the mean free flow $u_0 = \mathrm{Ma}\sqrt{\gamma}$ is tuned to check the capability of the present method to transport on a relatively

long distance. Ma $= 4, 3, 2, 1$ are chosen along with CFL $= 0.1,\ 0.15,\ 0.2,\ 0.3$ to ensure stability. The hybrid weighting parameter is fixed to $\sigma = 1$, meaning that the stress tensor is completely recovered from the LB scheme. The analytical solution of this Euler simulation is a frozen vortex advected without any dissipation nor dispersion. Therefore, a vanishing $\mu = 10^{-15}$ viscosity is chosen to mimic an Euler solver. The initial solution is

$$\rho = \left[1 - \frac{(\gamma-1)}{2} M_v^2 e^{1-r^2/R^2}\right]^{\frac{1}{\gamma-1}}, \quad p = \rho^\gamma, \tag{76}$$

$$u = u_0 - M_v\sqrt{\gamma}\, e^{(1-r^2/R^2)/2}\,(y - y_c)\,, \tag{77}$$

$$v = M_v\sqrt{\gamma}\, e^{(1-r^2/R^2)/2}\,(x - x_c)\,, \tag{78}$$

with $M_v = 1/(4\pi\sqrt{\gamma})$. Density fields after exactly 20 periods are plotted on Figure 1, it is seen that the overall circular shape is well conserved by the present solver, even after a relatively long distance of $200R$. To further validate the present results, $y = 5$ slices for different Ma numbers are also plotted on Figure 2, showing that while higher Ma values led to higher errors, the damping remained very small for Mach numbers up to Ma $= 4$, exhibiting less than 6% of errors when compared to the reference analytical solution.

B. Entropy spot

This second test case is very similar to the isentropic vortex except that we now transport an entropy spot, initialized as

$$\rho = \left(1 + \epsilon e^{-r^2/R^2}\right), \tag{79}$$

$$p = 1\,, \qquad u = u_0\,, \qquad v = 0\,. \tag{80}$$

The analytical solution is also a frozen pattern advected by the mean flow $u_0 = \mathrm{Ma}\sqrt{\gamma}$ without any changes of shape or amplitude. All the other numerical and physical parameters are exactly the same as those of the isentropic vortex. Figure 3 presents a comparison between different Ma values. After 20 periods the circular shape is well preserved. $y = 5$ slices can be seen on Figure 4 to quantitatively show how the numerical errors introduced by the present method altered the entropy spot. Again, higher Mach led to more damping, but it remained in an acceptable margin of about 5% errors. Note that the choice of the numerical MUSCL-Hancock scheme for the convective term of Eq.(66) is of critical importance for this test case as it can be seen on

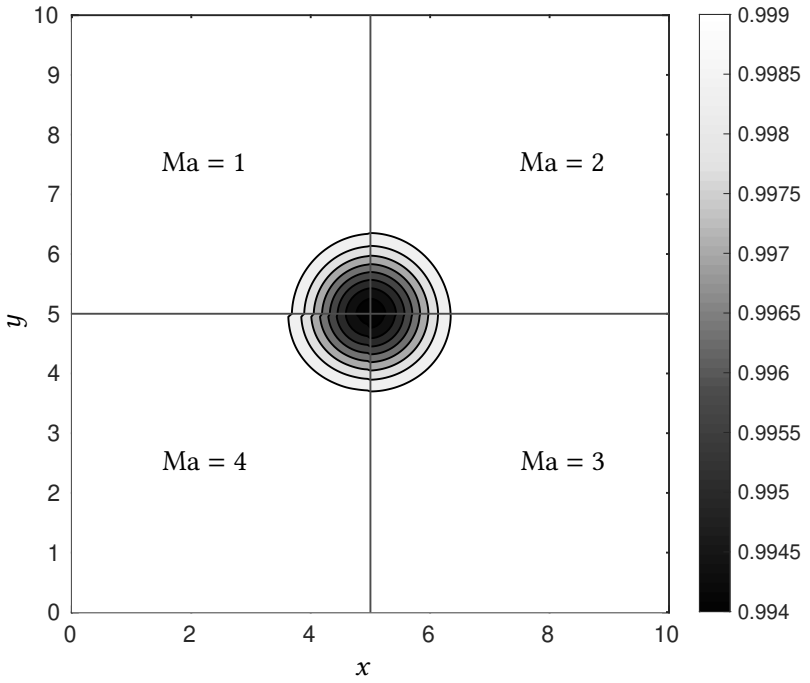

Figure 1: Isentropic vortex : Isotropy comparison after 20 convective times at different Mach numbers.

Figure 5, where different numerical schemes were employed for the Ma = 1 case. It is shown that the accurate transport of the entropy mode significantly depends on the discretization of Eq.(66), highlighting that numerical properties of Hybrid LB schemes are inherited from both the LB part and FD part.

C. Thermal Couette flow

In this test case, a $H = 1\times10^{-4}$ long domain is discretized by a 1×100 grid. Prandtl number Pr is fixed to 0.71. The adiabatic exponent is chosen as $\gamma = 1.4$. Characteristic CFL ranges from 0.2 to 0.5 to ensure the stability of the simulations while the hybrid LB parameter is fixed to $\sigma = 0.9$. A no-slip isothermal wall moving at $Ma = 1.3, 2.3, 3.3$ is placed at $y = H$, and a no-slip wall at $y = 0$, leading to a linear velocity profile with constant shear-stress. Due to the viscous heat term present in the entropy equation Eq.(66) the fluid is heated up. When the generated heat is balanced by heat diffusion, a stationary solution is achieved. The Reynolds number does not change the stationary analytical solution, but it controls the rate of momentum transfer from

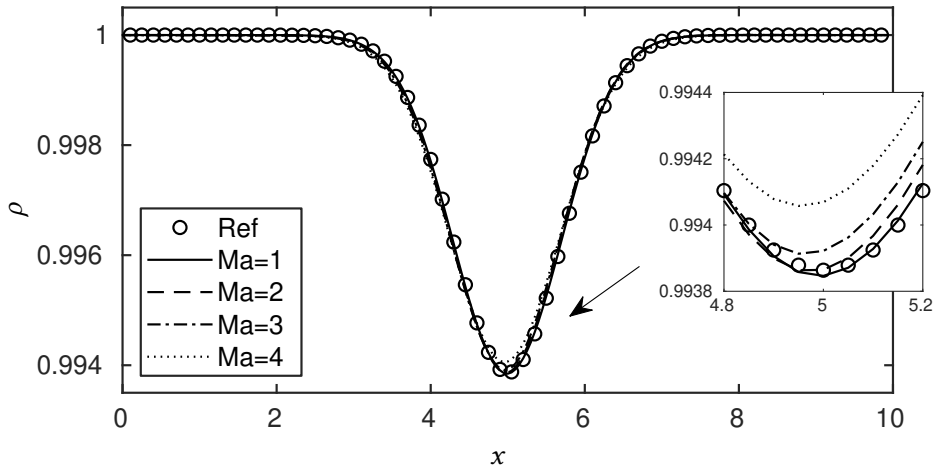

Figure 2: Isentropic vortex : Comparison of $y = 0$ density slices at different Mach numbers after 20 periods.

the moving wall to the inner domain. A Reynolds number of order unity is therefore chosen to allow a fast convergence, after which a constant $\mathcal{L}_2$ error for temperature and velocity fields of order 1×10^{-3} and 1×10^{-4} are reported for all Mach numbers tested. In Figure 6, the normalized temperature and normalized velocity curves are compared to their analytical counterparts[13]. A satisfactory agreement is observed for both profiles, showing the capability of the present model to handle viscous and heat conduction terms.

D. 2D Riemann problems

To assess the capability of the present solver to handle discontinuities in a wide range of situations, configurations 4-6-11-12-13-16 in[43] are simulated with the same numerical parameters. These test cases are 2D Riemann problems, they are initialized by 4 constant states divided by discontinuities placed along $x = 0.5$ and $y = 0.5$. The exact initial conditions are given in Appendix D.

The LB parameter is fixed to $\sigma = 1.0$, a square domain of side length $L = 1$ is discretized by a 400×400 grid. Dynamic viscosity is fixed to $\mu = 10^{-15}$ while the adiabatic exponent is $\gamma = 1.4$. Similarly to[43], a fixed value of $\Delta t/\Delta x = 0.22$ is chosen here. Density fields are presented after 500 timesteps for all 6 configurations in Figure 7 where 50 isolines are linearly ranging from $1.05 \times \min(\rho)$ to $0.95 \times \max(\rho)$. The shock sensor parameter is fixed to $s_c = 0.3$ to reduce Gibbs oscillations near discontinuities. The shape of the complex patterns of shocks, contact

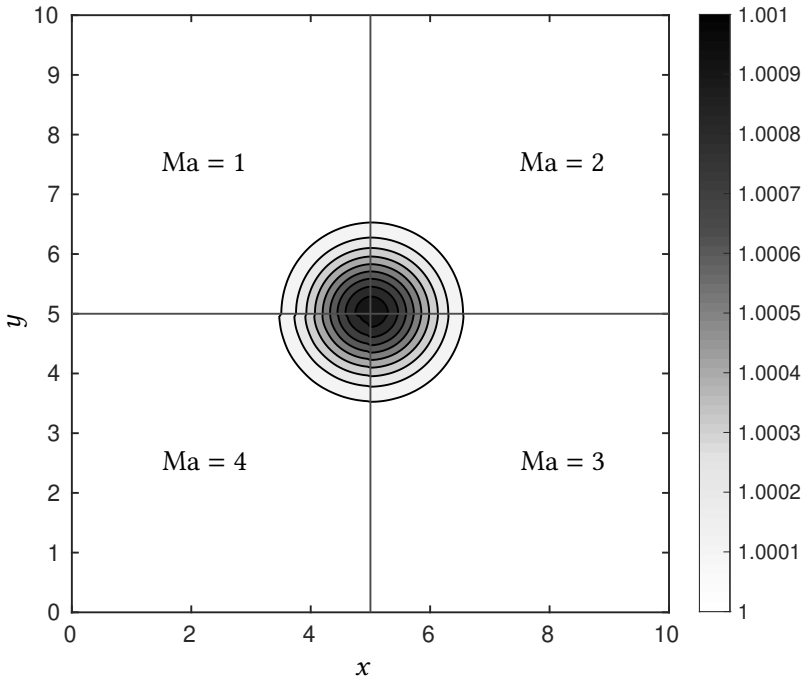

Figure 3: Entropy spot : Isotropy comparison after 20 convective times at different Mach numbers.

discontinuities and rarefaction waves presented in[43] are well reproduced in all 6 configurations.

E. Compressible double shear layer

To further demonstrate the stability of the proposed solver, a compressible double shear layer problem is specifically designed and tested on different square grids. The fully periodic square $[L \times L]$ domain is discretized by 64×64, 128×128, 256×256, 512×512 and 1024×1024 grids and the initial CFL is fixed to $CFL = 0.28$. For this simulation, $\sigma = 1$ is used. Adiabatic exponent is $\gamma = 1.4$, dynamic viscosity is taken as $\mu = 10^{-15}$ to model an Euler simulation, characteristic Mach number is Ma $= 0.65$ and the simulation is run until $2t_c = \frac{2L}{\text{Ma}\sqrt{\gamma}}$. The initial solution,

$$u = \begin{cases} \text{Ma}\sqrt{\gamma}\tanh k(y - 0.25)\,, & \text{if } y \leq 0.5 \\ \text{Ma}\sqrt{\gamma}\tanh k(0.75 - y)\,, & \text{if } y > 0.5 \end{cases} \tag{81}$$

$$v = \text{Ma}\sqrt{\gamma}\delta \sin 2\pi(x + 0.25)\,, \quad \rho = 1\,, \quad T = 1\,, \tag{82}$$

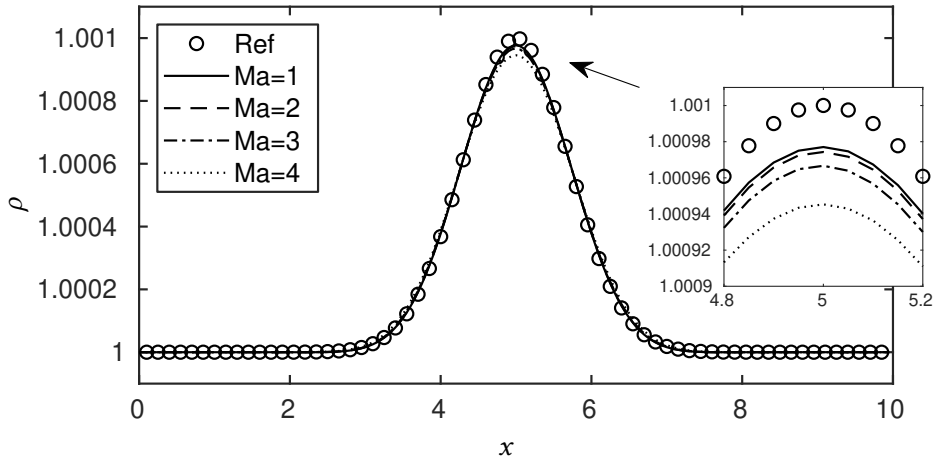

Figure 4: Entropy spot : Comparison of $y = 0$ density slices at different Mach numbers after 20 periods.

is made of two layers of fluid sliding on each other through a sigmoidal profile of characteristic thickness $k = 80$. A sinusoidal perturbation whose amplitude is controlled by $\delta = 0.05$ by introduced on the spanwise velocity, which eventually leads to the formation of a clockwise and counter-clockwise vortices around $t = t_c$, local Mach number then exceeds its inital value. Because the chosen initial Mach number is sufficiently large, a complex pattern of 4 radial shocks is formed around time $t = 2t_c$ and interacts with the circumferential slip lines wrapping around each vortex. This can be seen on Figure 8, where vorticity and Mach fields are represent at $t = (t_c, 2t_c)$ for the 512×512 grid. A quantitative comparison between different grids can be seen on Figure 9, where vorticity and Mach are plotted along the diagonal line of the bottom left quadrant. No sensor viscosity is used in this test case, therefore, the stability of the simulation completely relies on the numerical viscosity and hyperviscosity introduced by truncature errors.

F. Shock-vortex interaction

The shock-vortex interaction is a complex test case in which both accuracy and stability are tested. The simulation is characterized by a $Ma = 1.2$ stationary shock positioned at $x_s = 8$ and initialized by the Rankine-Hugoniot jump conditions,

$$\frac{\rho_R}{\rho_L} = \frac{u_L}{u_R} = \frac{(\gamma+1)Ma^2}{(\gamma-1)Ma^2+2}, \qquad \frac{p_R}{p_L} = 1 + \frac{2\gamma}{(\gamma+1)}(Ma^2-1)\,. \tag{83}$$

In the unshocked region is superimposed a $M_v = 0.25$ isentropic vortex Eq.(76). Other physical parameters are set to $\gamma = 1.4$, $Re = 800$, $Pr = 0.75$, $p_L = 1.0$, $T_L = 1.0$, $u_L = M_s\sqrt{\gamma}$. The simulation takes place in a $[0, 28] \times [0, 24]$ computational domain discretized by a 1120×960 grid. The initial position of the vortex is $(x_c, y_c) = (6, 12)$. The maximum CFL, evaluated in the unshocked region, is set to 0.83 and the stabilizing parameter of the hybrid lattice Boltzmann model is $\sigma = 0.7$.

On Fig. 10 is plotted the normalized pressure fluctuation $\Delta p = \frac{p - p_R}{p_R}$ along a radial slice of angle $\theta = -45°$ at different integer multiples of the characteristic time $T = \frac{R}{c_R}$ corresponding to $t = 6T$, $t = 8T$ and $t = 10T$. A circumferential slice around the vortex at time $t = 6T$ is also visible for two different radii. Both the radial and circumferential slices are in good agreement with the reference solution.

G. Shock-entropy spot interaction

Similarly to the shock-vortex interaction, a stationary shock is placed at $x_s = 10$. The mean flow is initialized through the Rankine-Hugoniot jump conditions Eqs.(83). An entropy spot of amplitude $\epsilon = 0.1$, centered at $(x_c, y_c) = (3, 12)$ is placed in the unshocked region. Note that $|x_s - x_c|$ is more than 3 times higher than for the last test case to avoid any superposition of the initial profiles of shock and entropy-spot. Other relevant parameters are set to $\mu = 10^{-15}$, $p_L = 1.0$, $T_L = 1.0$, $u_L = M_s\sqrt{\gamma}$ and $s_c = 0$. Domain and numerical parameters such as Δx and σ are identical to the shock-vortex test case, with a lower value of the timestep characterized by CFL $= 0.42$. The simulation is run until $t = 8$, for three different values of the adiabatic exponent, $\gamma = 1.2,\ 1.4,\ 1.6$. During the simulation, the pure entropy spot crosses the shock wave and creates and pattern of frozen entropy, frozen vorticity and pressure waves[45,46]. Frozen modes are plotted in the frame reference of the shocked spot on Figure 11 and Figure 12 while the pressure non-evanescent field is plotted on Figure 13 in the frame reference of the shock. On all these figures, negative y corresponds to analytical solutions[45,46] while positive y corresponds to the present solver. Isolines are in excellent agreement for all three fields, except for some very small discrepancies observed on vorticity fields along the $x = 0$ line.

V. CONCLUSION

A unified formulation for segregated improved density-based and pressure-based LBM-BGK methods has been proposed. It is shown that in the absence of forcing term these approaches are identical. By reinstating the force term, several preexisting LB models are then recovered as special cases of this generalized formulation by tuning free fields ζ and κ in the equilibrium distribution, corresponding to changes in third and fourth order moments. In the context of hybrid recursive regularized models, those free fields mainly drive non-hydrodynamic consistency defects in the stress-tensor equation[17], but also numerical errors and stability of the present solver.

Then a segregated compressible method based on this unified approach has been built using the HRR approach. Coupled with an entropy evolution equation, this model is able to model subsonic to supersonic flows.

Its efficiency for high speed compressible flows has been assessed considering a broad range of test cases and physical parameters, illustrating the stability of the proposed method.

ACKNOWLEDGEMENTS

We thank T. Lafarge for inspiring discussions.

Part of this research was supported by ANR, Renault, Airbus and SafranTech by the Industrial Chair Program ALBUMS (ANR-CHIND-18-ALBUMS). Centre de Calcul Intensif d'Aix-Marseille is acknowledged for granting access to their high performance computing resources. We also acknowledge support from Labex MEC (ANR-10-LABX-0092) and the A*MIDEX project (ANR-11-IDEX-0001-02), funded by the "Investissements d'Avenir".

Appendix A: D3Q19r basis

The D3Q19r rotational symmetry basis of Gauss-Hermite polynomials detailed in[35] and used in this study reads as

$$\mathcal{H}_{i}^{(0)} \equiv 1\,, \tag{A1a}$$

$$\mathcal{H}_{i,\alpha}^{(1)} \equiv c_{i\alpha}\,, \tag{A1b}$$

$$\mathcal{H}_{i,\alpha\beta}^{(2)} \equiv c_{i\alpha}c_{i\beta} - c_s^2\delta_{\alpha\beta}\,, \tag{A1c}$$

$$\mathcal{H}_{i,\alpha\beta\gamma}^{(3)} \equiv c_{i\alpha}c_{i\beta}c_{i\gamma} - c_s^2(\delta_{\alpha\beta}c_{i\gamma} + \delta_{\beta\gamma}c_{i\alpha} + \delta_{\alpha\gamma}c_{i\beta})\,, \tag{A1d}$$

$$\begin{aligned}\mathcal{H}_{i,\alpha\beta\gamma\delta}^{(4)} \equiv\ & c_{i\alpha}c_{i\beta}c_{i\gamma}c_{i\delta} + c_s^4(\delta_{\alpha\beta}\delta_{\gamma\delta} + \delta_{\beta\gamma}\delta_{\delta\alpha} + \delta_{\delta\alpha}\delta_{\beta\gamma}) \\ & - c_s^2(c_{i\alpha}c_{i\beta}\delta_{\gamma\delta} + c_{i\beta}c_{i\gamma}\delta_{\delta\alpha} + c_{i\gamma}c_{i\delta}\delta_{\alpha\beta} + c_{i\delta}c_{i\alpha}\delta_{\beta\gamma} + c_{i\gamma}c_{i\alpha}\delta_{\beta\delta} + c_{i\beta}c_{i\delta}\delta_{\alpha\gamma})\,,\end{aligned} \tag{A1e}$$

$$\mathcal{H}_{i,1}^{(3r)} \equiv \mathcal{H}_{i,xxy}^{(3)} + \mathcal{H}_{i,yzz}^{(3)}\,, \tag{A1f}$$

$$\mathcal{H}_{i,2}^{(3r)} \equiv \mathcal{H}_{i,xzz}^{(3)} + \mathcal{H}_{i,xyy}^{(3)}\,, \tag{A1g}$$

$$\mathcal{H}_{i,3}^{(3r)} \equiv \mathcal{H}_{i,yyz}^{(3)} + \mathcal{H}_{i,xxz}^{(3)}\,, \tag{A1h}$$

$$\mathcal{H}_{i,4}^{(3r)} \equiv \mathcal{H}_{i,xxy}^{(3)} - \mathcal{H}_{i,yzz}^{(3)}\,, \tag{A1i}$$

$$\mathcal{H}_{i,5}^{(3r)} \equiv \mathcal{H}_{i,xzz}^{(3)} - \mathcal{H}_{i,xyy}^{(3)}\,, \tag{A1j}$$

$$\mathcal{H}_{i,6}^{(3r)} \equiv \mathcal{H}_{i,yyz}^{(3)} - \mathcal{H}_{i,xxz}^{(3)}\,. \tag{A1k}$$

Leading to 16 linearly independant Hermite polynomials. To form a complete basis, 3 additional orthogonal polynomials should be defined,

$$\mathcal{A}_i = \frac{4}{9}\left(3 + 2\sqrt{3}\right)\mathcal{D}_{xyz}^{(4)} + \frac{4}{9}\left(3 - \sqrt{3}\right)\mathcal{D}_{xzy}^{(4)} + \frac{4}{9}\left(3 - \sqrt{3}\right)\mathcal{D}_{zyx}^{(4)}\,, \tag{A2}$$

$$\mathcal{B}_i = \frac{4}{9}\left(3 + 2\sqrt{3}\right)\mathcal{D}_{xzy}^{(4)} + \frac{4}{9}\left(3 - \sqrt{3}\right)\mathcal{D}_{xyz}^{(4)} + \frac{4}{9}\left(3 - \sqrt{3}\right)\mathcal{D}_{zyx}^{(4)}\,, \tag{A3}$$

$$C_i = \frac{4}{9}\left(3 + 2\sqrt{3}\right)\mathcal{D}_{zyx}^{(4)} + \frac{4}{9}\left(3 - \sqrt{3}\right)\mathcal{D}_{xzy}^{(4)} + \frac{4}{9}\left(3 - \sqrt{3}\right)\mathcal{D}_{xyz}^{(4)}\,, \tag{A4}$$

where $\mathcal{D}_{xyz}^{(4)} = \mathcal{H}_{ixxyy}^{(4)} + \frac{c_s^2}{2}\mathcal{H}_{izz}^{(2)}$. Additionally, let's remark that

$$\sum_i \omega_i \mathcal{A}_i\mathcal{A}_i = \sum_i \omega_i \mathcal{B}_i\mathcal{B}_i = \sum_i \omega_i C_i C_i = 24c_s^8\,. \tag{A5}$$

And the Hermite moments corresponding to this rotated basis are

$$a^{(0)} \equiv \sum_i \mathcal{H}_i^{(0)} f_i \,, \tag{A6a}$$

$$a_\alpha^{(1)} \equiv \sum_i \mathcal{H}_{i,\alpha}^{(1)} f_i \,, \tag{A6b}$$

$$a_{\alpha\beta}^{(2)} \equiv \sum_i \mathcal{H}_{i,\alpha\beta}^{(2)} f_i \,, \tag{A6c}$$

$$a_{\alpha\beta\gamma}^{(3)} \equiv \sum_i \mathcal{H}_{i,\alpha\beta\gamma}^{(3)} f_i \,, \tag{A6d}$$

$$a_1^{(3r)} \equiv 3\left(a_{xxy}^{(3)} + a_{yzz}^{(3)}\right) , \tag{A6e}$$

$$a_2^{(3r)} \equiv 3\left(a_{xzz}^{(3)} + a_{xyy}^{(3)}\right) , \tag{A6f}$$

$$a_3^{(3r)} \equiv 3\left(a_{yyz}^{(3)} + a_{xxz}^{(3)}\right) , \tag{A6g}$$

$$a_4^{(3r)} \equiv a_{xxy}^{(3)} - a_{yzz}^{(3)} \,, \tag{A6h}$$

$$a_5^{(3r)} \equiv a_{xzz}^{(3)} - a_{xyy}^{(3)} \,, \tag{A6i}$$

$$a_6^{(3r)} \equiv a_{yyz}^{(3)} - a_{xxz}^{(3)} \,, \tag{A6j}$$

$$a_{\mathcal{A}}^{(4)} \equiv \sum_i \mathcal{A}_i f_i \,, \tag{A6k}$$

$$a_{\mathcal{B}}^{(4)} \equiv \sum_i \mathcal{B}_i f_i \,, \tag{A6l}$$

$$a_C^{(4)} \equiv \sum_i C_i f_i \,. \tag{A6m}$$

Therefore, on D3Q19r, any function f_i can be written as

$$f_i = w_i \left\{ \sum_{n=0}^{2} \frac{1}{n! c_s^{2n}} a^{(n)} : \mathcal{H}_i^{(n)} + \frac{\mathcal{H}_{i\gamma}^{(3r)}}{6c_s^6} a_\gamma^{(3r)} + \frac{\mathcal{A}_i a_{\mathcal{A}}^{(4)} + \mathcal{B}_i a_{\mathcal{B}}^{(4)} + C_i a_C^{(4)}}{24 c_s^8} \right\} . \tag{A7}$$

Note that an equivalent orthogonal D3Q19r basis can also be found in[47].

Appendix B: Further details about the comparison of both models

1. Non-equilibrium definition in p-based

The equivalence between models was obtained by a straight comparison of the numerical schemes corresponding to the p-based model (Section II B) and the improved ρ-based model (Section II C). In this demonstration it was implicitly assumed that the whole numerical solution

can be summarized by the knowledge of moments $[\rho, \rho u_\alpha, \theta, \Pi^{neq}_{\alpha\beta}]$, which is true for regularized collisions[33,34]. However, for other kernels, higher order moments ($\Pi_{\alpha\beta\gamma}$, $\Pi_{\alpha\beta\gamma\delta}$, ...) should also be considered. Here, we provide a general demonstration of the equivalence between the two models presented in Sections II C and II B on the BGK collision kernel. This collision kernel is the simplest one in which the knowledge of moments $[\rho, \rho u_\alpha, \theta, \Pi^{neq}_{\alpha\beta}]$ is insufficient to reconstruct the complete numerical solution for an arbitrary lattice. First, let's notice that in classical LB models, mass conservation requires

$$\sum_i \left[\overline{f}_i - f_i^{eq}\right] = 0\,. \tag{B1}$$

As a consequence, classically, second order non-equilibrium raw $\Pi^{neq}_{\alpha\beta}$ and Hermite $a^{neq}_{\alpha\beta}$ moments follow

$$\Pi^{neq}_{\alpha\beta} = a^{neq}_{\alpha\beta}\,. \tag{B2}$$

On the contrary, in p-based model, because of Eq.(10), the definition of the updated density can be recast as

$$\sum_i \left(\overline{f}_i^p - f_i^{p,eq}\right)(t,\boldsymbol{x}) + \left[\rho(t,\boldsymbol{x})(\theta(t,\boldsymbol{x})-1) - \rho(t-\Delta t,\boldsymbol{x})(\theta(t-\Delta t,\boldsymbol{x})-1)\right] = 0\,, \tag{B3}$$

or equivalently,

$$\sum_i \left\{\left(\overline{f}_i^p - f_i^{p,eq,}\right)(t,\boldsymbol{x}) + \delta_{i0}\left[\rho(t,\boldsymbol{x})(\theta(t,\boldsymbol{x})-1) - \rho(t-\Delta t,\boldsymbol{x})(\theta(t-\Delta t,\boldsymbol{x})-1)\right]\right\} = 0\,, \tag{B4}$$

where δ_{i0} is a Kroenecker symbol. A comparison of this last equation with Eq.(B1) pleads for a different definition of p-based non-equilibrium distribution. Instead of the classical $\overline{f}_i^p - f_i^{p,eq}$, non-equilibrium distribution can now be defined as

$$\begin{aligned}\overline{f}_i^{p,neq}(t,\boldsymbol{x}) = &\left(\overline{f}_i^p - f_i^{p,eq}\right)(t,\boldsymbol{x}) \\ &+ \delta_{i0}\left[\rho(t,\boldsymbol{x})(\theta(t,\boldsymbol{x})-1) - \rho(t-\Delta t,\boldsymbol{x})(\theta(t-\Delta t,\boldsymbol{x})-1)\right]\,.\end{aligned} \tag{B5}$$

This definition of the non-equilibrium verifies

$$\Pi^{neq}_{\alpha\beta} = \sum_i c_{i\alpha}c_{i\beta}\overline{f}_i^{p,neq} = \sum_i \mathcal{H}^{(2)}_{i\alpha\beta}\overline{f}_i^{p,neq} = a^{neq}_{\alpha\beta}\,. \tag{B6}$$

However, in either[13] or Section II B, Eq.(B5) was never used. Instead, raw and Hermite moments classically read in p-based as

$$\sum_i \mathcal{H}^{(2)}_{i\alpha\beta}\left[\overline{f}_i^p - f_i^{p,eq}\right] \neq \sum_i c_{i\alpha}c_{i\beta}\left[\overline{f}_i^p - f_i^{p,eq}\right]\,. \tag{B7}$$

This does not seem to be consistent with Eq.(B2). This ambiguity is eliminated by noting that the computation of both $a^{neq}_{\alpha\beta}$ and $\Pi^{neq}_{\alpha\beta}$ is unnecessary in regularized LB algorithms, only raw moments $\Pi^{neq}_{\alpha\beta}$ are necessary. Therefore, defining Hermite moments from raw moments $a^{neq}_{\alpha\beta} \equiv \Pi^{neq}_{\alpha\beta}$ as in both[17] and Section II B or traceless second order Hermite moments $a^{neq}_{\alpha\beta} \equiv \sum_i [c_{i\alpha}c_{i\beta} - \frac{\delta_{\alpha\beta}}{3}c_{i\gamma}c_{i\gamma}](\overline{f}_i - f_i^{\mathrm{eq}})$ as in[13] instead of Hermite moments allows to bypass the unusual definition Eq.(B5). Instead, the non-equilibrium remains defined as

$$\overline{f}_i^{p,neq}(t,\boldsymbol{x}) \equiv (\overline{f}_i^{p} - f_i^{p,eq})(t,\boldsymbol{x})\,. \tag{B8}$$

With the natural definition of non-equilibrium Eq.(B5) for an arbitrary kernel, let's try to compare our two models using the more classical BGK collision kernel, in which Eq.(B5) would lead to inconsistent results.

2. Consistent BGK p-based

A p-based model equipped with non-equilibrium Eq.(B5) reads

$$\begin{aligned}\overline{f}_i^{p}(t+\Delta t,\boldsymbol{x}) = f_i^{eq,p}(t,\boldsymbol{x}-\boldsymbol{c}_i\,\Delta t) + \left(1-\frac{\Delta t}{\tau+\Delta t/2}\right)\Big\{&\overline{f}_i^{p}(t,\boldsymbol{x}-\boldsymbol{c}_i\,\Delta t) - f_i^{eq,p}(t,\boldsymbol{x}-\boldsymbol{c}_i\,\Delta t)\\ &- \delta_{0i}\left[[\rho(\theta-1)](t-\Delta t,\boldsymbol{x}) - [\rho(\theta-1)](t,\boldsymbol{x})\right]\Big\}\,.\end{aligned} \tag{B9}$$

Then, by adding on both sides $-\delta_{0i}[\rho(\theta-1)](t,\boldsymbol{x})$ we get,

$$\begin{aligned}&\overline{f}_i^{p}(t+\Delta t,\boldsymbol{x}) - \delta_{0i}[\rho(\theta-1)](t,\boldsymbol{x}) = f_i^{eq,p}(t,\boldsymbol{x}-\boldsymbol{c}_i\,\Delta t) - \delta_{0i}[\rho(\theta-1)](t,\boldsymbol{x})\\ &+\left(1-\frac{\Delta t}{\tau+\Delta t/2}\right)\Big\{\overline{f}_i^{p}(t,\boldsymbol{x}-\boldsymbol{c}_i\,\Delta t) - f_i^{eq,p}(t,\boldsymbol{x}-\boldsymbol{c}_i\,\Delta t)\\ &- \delta_{0i}\left[[\rho(\theta-1)](t-\Delta t,\boldsymbol{x}) - [\rho(\theta-1)](t,\boldsymbol{x})\right]\Big\}\,.\end{aligned} \tag{B10}$$

Using Eqs.(20), (23) we finally get

$$\overline{f}_i^{\rho}(t+\Delta t,\boldsymbol{x}) = f_i^{eq,\rho}(t,\boldsymbol{x}-\boldsymbol{c}_i\,\Delta t) + \left(1-\frac{\Delta t}{\tau+\Delta t/2}\right)\Big\{\overline{f}_i^{\rho}(t,\boldsymbol{x}-\boldsymbol{c}_i\,\Delta t) - f_i^{eq,\rho}(t,\boldsymbol{x}-\boldsymbol{c}_i\,\Delta t)\Big\}\,, \tag{B11}$$

with the equilibrium defined as Eq.(13), which is nothing else than the improved ρ-based model equipped with a BGK collision kernel. This definition formally proves the exact equivalence between improved ρ-based and a p-based equipped by Eq.(B5) on BGK collision kernel.

Appendix C: Appendix : Finite difference operators

1. MUSCL-Hancock method

Convective part of the entropy equation is discretized as follows

$$\frac{s_i^{n+1} - s_i^n}{\Delta t} + \frac{F(s^n_{i+\frac{1}{2}}) - F(s^n_{i-\frac{1}{2}})}{\Delta x} = 0. \tag{C1}$$

Where $F(s^n_{i+\frac{1}{2}})$ and $F(s^n_{i-\frac{1}{2}})$ are computed using the following steps :

i) Extrapolated intercell values are evaluated at the left and right sides of the ith cell as

$$s_{i,L} = s_i - \frac{1}{2}\Delta_i\,, \qquad s_{i,R} = s_i + \frac{1}{2}\Delta_i\,, \tag{C2}$$

with Δ_i a high order approximation of the slope,

$$\Delta_i = \frac{1}{2}\left[(1+\eta)\,(s_i - s_{i-1}) + (1-\eta)\,(s_{i+1} - s_i)\right]\,, \tag{C3}$$

and $\eta = \frac{1}{3}\left[\frac{2\,\Delta t\,u_i}{\Delta x} - \mathrm{sign}(u_i)\right]$ as suggested in[41].

ii) Evolving of extrapolated boundary values by a time $\frac{\Delta t}{2}$ is done by

$$\bar{s}_{i,L} = s_{i,L} + \frac{\Delta t\,u_i}{2\Delta x}\left(s_{i,L} - s_{i,R}\right)\,, \qquad \bar{s}_{i,R} = s_{i,R} + \frac{\Delta t\,u_i}{2\Delta x}\left(s_{i,L} - s_{i,R}\right)\,. \tag{C4}$$

iii) Then $F(s^n_{i+\frac{1}{2}})$ and $F(s^n_{i-\frac{1}{2}})$ are evaluated as

$$F(s^n_{i+\frac{1}{2}}) = \begin{cases} u_i\,\bar{s}_{i,R} & \text{if } u_i \geq 0 \\ u_i\,\bar{s}_{i+1,L} & \text{if } u_i < 0 \end{cases} \qquad F(s^n_{i-\frac{1}{2}}) = \begin{cases} u_i\,\bar{s}_{i-1,R} & \text{if } u_i \geq 0 \\ u_i\,\bar{s}_{i,L} & \text{if } u_i < 0 \end{cases} \tag{C5}$$

For passive scalar advection, this scheme results in a compact 5 points stencil which is $O(\Delta t^3, \Delta x^3)$ accurate[41].

2. Other schemes

Temporal gradients of the dummy variable ϕ in the force corrective term F_i are discretized using an $O(\Delta t)$ accurate Euler operator

$$\frac{\partial \phi}{\partial t} \approx \frac{\phi(t) - \phi(t - \Delta t)}{\Delta t}\,, \tag{C6}$$

while spatial gradients are systematically discretized by a $O(\Delta x)$ accurate upwind schemes[24],

$$\frac{\partial \phi}{\partial x} \approx \begin{cases} \dfrac{\phi(x) - \phi(x - \Delta x)}{\Delta x} & \text{if } u_x \geq 0 \\ \dfrac{\phi(x + \Delta x) - \phi(x)}{\Delta x} & \text{if } u_x < 0 \end{cases} , \tag{C7}$$

except for the velocity divergence operator which is discretized similarly to the viscous heat using an $O(\Delta x^2)$ accurate centered scheme,

$$\frac{\partial \phi}{\partial x} \approx \frac{\phi(x + \Delta x) - \phi(x - \Delta x)}{2\,\Delta x} . \tag{C8}$$

Using the chain rule, the heat conduction term in Eq.(66) is recast in a sum of a product of first order gradients discretized by Eq.(C8) and a laplacian operator discretized by an $O(\Delta x^2)$ accurate centered scheme,

$$\frac{\partial^2 \phi}{\partial x^2} \approx \frac{\phi(x + \Delta x) - 2\phi(x) + \phi(x - \Delta x)}{\Delta x^2} . \tag{C9}$$

Appendix D: Appendix : 2D Riemann initial states

We provide in this appendix all initial states[43] used in Section IV D for the chosen two dimensional Riemann problems.

$$(p,\rho,u,v)_{\text{Config.4}} = \begin{cases} (1.1, 1.1, 0.0, 0.0) & \text{if } x \geq 0.5,\ y \geq 0.5 \\ (0.35, 0.5065, 0.8939, 0.0) & \text{if } x < 0.5,\ y \geq 0.5 \\ (1.1, 1.1, 0.8939, 0.8939) & \text{if } x < 0.5,\ y < 0.5 \\ (0.35, 0.5065, 0.0, 0.8939) & \text{if } x \geq 0.5,\ y < 0.5 \end{cases} \tag{D1}$$

$$(p,\rho,u,v)_{\text{Config.6}} = \begin{cases} (1.0, 1.0, 0.75, -0.5) & \text{if } x \geq 0.5,\ y \geq 0.5 \\ (1.0, 2.0, 0.75, 0.5) & \text{if } x < 0.5,\ y \geq 0.5 \\ (1.0, 1.0, -0.75, 0.5) & \text{if } x < 0.5,\ y < 0.5 \\ (1, 3, -0.75, -0.5) & \text{if } x \geq 0.5,\ y < 0.5 \end{cases} \tag{D2}$$

$$(p,\rho,u,v)_{\text{Config.11}} = \begin{cases} (1.0, 1.0, 0.1, 0.0) & \text{if } x \geq 0.5,\ y \geq 0.5 \\ (0.4, 0.5313, 0.8276, 0.0) & \text{if } x < 0.5,\ y \geq 0.5 \\ (0.4, 0.8, 0.1, 0.0) & \text{if } x < 0.5,\ y < 0.5 \\ (0.4, 0.5313, 0.1, 0.7276) & \text{if } x \geq 0.5,\ y < 0.5 \end{cases} \tag{D3}$$

$$(p,\rho,u,v)_{\text{Config.12}} = \begin{cases} (0.4, 0.5313, 0.0, 0.0) & \text{if } x \geq 0.5,\ y \geq 0.5 \\ (1.0, 1.0, 0.7276, 0.0) & \text{if } x < 0.5,\ y \geq 0.5 \\ (1.0, 0.8, 0.0, 0.0) & \text{if } x < 0.5,\ y < 0.5 \\ (1.0, 1.0, 0.0, 0.7276) & \text{if } x \geq 0.5,\ y < 0.5 \end{cases} \tag{D4}$$

$$(p,\rho,u,v)_{\text{Config.13}} = \begin{cases} (1.0, 1.0, 0.0, -0.3) & \text{if } x \geq 0.5,\ y \geq 0.5 \\ (1.0, 2.0, 0.0, 0.3) & \text{if } x < 0.5,\ y \geq 0.5 \\ (0.4, 1.0626, 0.0, 0.8145) & \text{if } x < 0.5,\ y < 0.5 \\ (0.4, 0.5313, 0.0, 0.4276) & \text{if } x \geq 0.5,\ y < 0.5 \end{cases} \tag{D5}$$

$$(p,\rho,u,v)_{\text{Config.16}} = \begin{cases} (0.4, 0.5313, 0.1, 0.1) & \text{if } x \geq 0.5,\ y \geq 0.5 \\ (1.0, 1.0222, -0.6179, 0.1) & \text{if } x < 0.5,\ y \geq 0.5 \\ (1.0, 0.8, 0.1, 0.1) & \text{if } x < 0.5,\ y < 0.5 \\ (1.0, 1.0, 0.1, 0.8276) & \text{if } x \geq 0.5,\ y < 0.5 \end{cases} \tag{D6}$$

DATA AVAILABILITY

The data that support the findings of this study are available from the corresponding author upon reasonable request.

REFERENCES

[1]T. Krüger, H. Kusumaatmaja, A. Kuzmin, O. Shardt, G. Silva, and E. M. Viggen, "The lattice boltzmann method," Springer International Publishing **10**, 978–3 (2017).

[2]Z. Guo and C. Shu, *Lattice Boltzmann method and its applications in engineering*, Vol. 3 (World Scientific, 2013).

[3]X. W. Shan, X. F. Yuan, and H. D. Chen, "Kinetic theory representation of hydrodynamics: a way beyond the Navier-Stokes equation," Journal of Fluid Mechanics **550**, 413–441 (2006).

[4]J. Jacob and P. Sagaut, "Wind comfort assessment by means of large eddy simulation with latice boltzmann method in full scale city area," Build. Environ. **139**, 110–124 (2018).

[5]L. Merlier, J. Jacob, and P. Sagaut, "Lattice-boltzmann large-eddy simulation of pollutant dispersion in street canyons including tree planting effects," Atmos. Environ. **195**, 89–103 (2018).

[6]L. Merlier, J. Jacob, and P. Sagaut, "Lattice-boltzmann large-eddy simulation of pollutant dispersion in complex urban environment with dense gas effect: Model evaluation and flow analysis," Build. Environ. **148**, 634–652 (2019).

[7]E. Buffa, J. Jacob, and P. Sagaut, "Lattice-boltzmann-based large-eddy simulation of high-rise building aerodynamics with inlet turbulence reconstruction," J. Wind Eng. Ind. Aerod. **212**, 104560 (2021).

[8]Y. Feng, J. Miranda-Fuentes, S. Guo, J. Jacob, and P. Sagaut, "Prolb: A lattice-boltzmann solver of large-eddy simulation of atmospheric boundary layer flows," Journal of Advances in Modelling Earth Systems **13**, e2020MS002107 (2021).

[9]O. Filippova and D. Haenel, "A novel lattice bgk approach for low mach number combustion," J. Comput. Phys. **158**, 139–160 (2000).

[10]O. Filippova and D. Haenel, "A novel numerical scheme for reactive flows at low mach numbers," Comput. Phys. Commun. **129**, 267–274 (2000).

[11]T. Inamuro, T. Ogata, T. S., and N. Konishi, "A lattice boltzmann method for incompressible two-phase flows with large density differences," J. Comput. Phys. **198**, 628–644 (2004).

[12]S. Mukherjee and J. Abraham, "A pressure-evolution-based multi-relaxation time high-density-ratio two-phase lattice-boltzmann model," Comput. Fluids **36**, 1149–1158 (2007).

[13]G. Farag, S. Zhao, T. Coratger, P. Boivin, G. Chiavassa, and P. Sagaut, "A pressure-based regularized lattice-boltzmann method for the simulation of compressible flows," Physics of Fluids **32**, 066106 (2020).

[14]M. Tayyab, B. Radisson, C. Almarcha, B. Denet, and P. Boivin, "Experimental and numerical lattice-boltzmann investigation of the darrieus–landau instability," Combustion and Flame **221**, 103–109 (2020).

[15]M. Tayyab, S. Zhao, and P. Boivin, "Lattice-boltzmann modeling of a turbulent bluff-body stabilized flame," Physics of Fluids **33**, 031701 (2021).

[16]I. Cheylan, S. Zhao, P. Boivin, and P. Sagaut, "Compressible pressure-based lattice-boltzmann applied to humid air with phase change," Applied Thermal Engineering **191**, 116868 (2021).

[17]G. Farag, S. Zhao, G. Chiavassa, and P. Boivin, "Consistency study of lattice-boltzmann schemes macroscopic limit," Physics of Fluids **33**, 037101 (2021).

[18]T. Astoul, G. Wissocq, J.-f. Boussuge, A. Sengissen, and P. Sagaut, "Lattice boltzmann method for computational aeroacoustics on non-uniform meshes: a direct grid coupling approach," arXiv preprint arXiv:2004.14887 (2020).

[19]B. J. Palmer and D. R. Rector, "Lattice-boltzmann algorithm for simulating thermal two-phase flow," Physical Review E **61**, 5295 (2000).

[20]B. J. Palmer and D. R. Rector, "Lattice boltzmann algorithm for simulating thermal flow in compressible fluids," Journal of Computational Physics **161**, 1–20 (2000).

[21]S. Guo, Y. Feng, and P. Sagaut, "Improved standard thermal lattice boltzmann model with hybrid recursive regularization for compressible laminar and turbulent flows," Physics of Fluids **32**, 126108 (2020).

[22]Y. Feng, P. Boivin, J. Jacob, and P. Sagaut, "Hybrid recursive regularized thermal lattice boltzmann model for high subsonic compressible flows," Journal of Computational Physics **394**, 82–99 (2019).

[23]S. Guo, Y. Feng, J. Jacob, F. Renard, and P. Sagaut, "An efficient lattice boltzmann method for compressible aerodynamics on d3q19 lattice," Journal of Computational Physics , 109570 (2020).

[24]F. Renard, Y. Feng, J.-F. Boussuge, and P. Sagaut, "Improved compressible hybrid lattice boltzmann method on standard lattice for subsonic and supersonic flows," Computers & Fluids **219**, 104867 (2021).

[25]F. Renard, G. Wissocq, J.-F. Boussuge, and P. Sagaut, "A linear stability analysis of compressible hybrid lattice boltzmann methods," arXiv preprint arXiv:2006.08477 (2020).

[26]G. Wissocq and P. Sagaut, "Hydrodynamic limits and numerical errors of isothermal lattice boltzmann schemes," (2021), arXiv:2104.14217 [physics.flu-dyn].

[27]R. J. LeVeque, *Finite difference methods for ordinary and partial differential equations: steady-state and time-dependent problems* (SIAM, 2007).

[28]P. L. Bhatnagar, E. P. Gross, and M. Krook, "A model for collision processes in gases. i. small amplitude processes in charged and neutral one-component systems," Physical review **94**, 511 (1954).

[29]N. Prasianakis, I. Karlin, J. Mantzaras, and K. Boulouchos, "Lattice boltzmann method with restored galilean invariance," Physical Review E **79**, 066702 (2009).

[30]M. H. Saadat, F. Bösch, and I. V. Karlin, "Lattice boltzmann model for compressible flows on standard lattices: Variable prandtl number and adiabatic exponent," Physical Review E **99**, 013306 (2019).

[31]M. Saadat, S. Hosseini, B. Dorschner, and I. Karlin, "Extended lattice boltzmann model for gas dynamics," Physics of Fluids **33**, 046104 (2021).

[32]R. Löhner, "Towards overcoming the les crisis," International Journal of Computational Fluid Dynamics **33**, 87–97 (2019).

[33]J. Latt and B. Chopard, "Lattice boltzmann method with regularized pre-collision distribution functions," Mathematics and Computers in Simulation **72**, 165–168 (2006).

[34]C. Coreixas, G. Wissocq, G. Puigt, J.-F. Boussuge, and P. Sagaut, "Recursive regularization step for high-order lattice boltzmann methods," Physical Review E **96**, 033306 (2017).

[35]J. Jacob, O. Malaspinas, and P. Sagaut, "A new hybrid recursive regularised bhatnagar–gross–krook collision model for lattice boltzmann method-based large eddy simulation," Journal of Turbulence **19**, 1051–1076 (2018).

[36]S. Zhao, G. Farag, P. Boivin, and P. Sagaut, "Toward fully conservative hybrid lattice boltzmann methods for compressible flows," Physics of Fluids **32**, 126118 (2020).

[37]L. D. Landau and E. M. Lifshitz, "Fluid mechanics," flme (1959).

[38]S. J. Blundell and K. M. Blundell, *Concepts in thermal physics* (OUP Oxford, 2009).

[39]O. Le Métayer and R. Saurel, "The noble-abel stiffened-gas equation of state," Physics of Fluids (1994-present) **28**, 046102 (2016).

[40]K. H. Kim, C. Kim, and O.-H. Rho, "Methods for the accurate computations of hypersonic flows: I. ausmpw+ scheme," Journal of Computational Physics **174**, 38–80 (2001).

[41]E. F. Toro, *Riemann solvers and numerical methods for fluid dynamics: a practical introduction* (Springer Science & Business Media, 2013).

[42]G. Wissocq, C. Coreixas, and J.-F. Boussuge, "Linear stability and isotropy properties of athermal regularized lattice boltzmann methods," Phys. Rev. E **102**, 053305 (2020).

[43]P. D. Lax and X.-D. Liu, "Solution of two-dimensional riemann problems of gas dynamics by positive schemes," SIAM Journal on Scientific Computing **19**, 319–340 (1998).

[44]O. Inoue and Y. Hattori, "Sound generation by shock–vortex interactions," J. Fluid Mech. **380**, 81–116 (1999).

[45]D. Fabre, L. Jacquin, and J. Sesterhenn, "Linear interaction of a cylindrical entropy spot with a shock," Physics of Fluids **13**, 2403–2422 (2001).

[46]G. Farag, P. Boivin, and P. Sagaut, "Interaction of two-dimensional spots with a heat releasing/absorbing shock wave: linear interaction approximation results," Journal of Fluid Mechanics **871**, 865–895 (2019).

[47]C. Coreixas, B. Chopard, and J. Latt, "Comprehensive comparison of collision models in the lattice boltzmann framework: Theoretical investigations," Physical Review E **100**, 033305 (2019).

(a) Lax-Wendroff[41]

(b) Fromm[41]

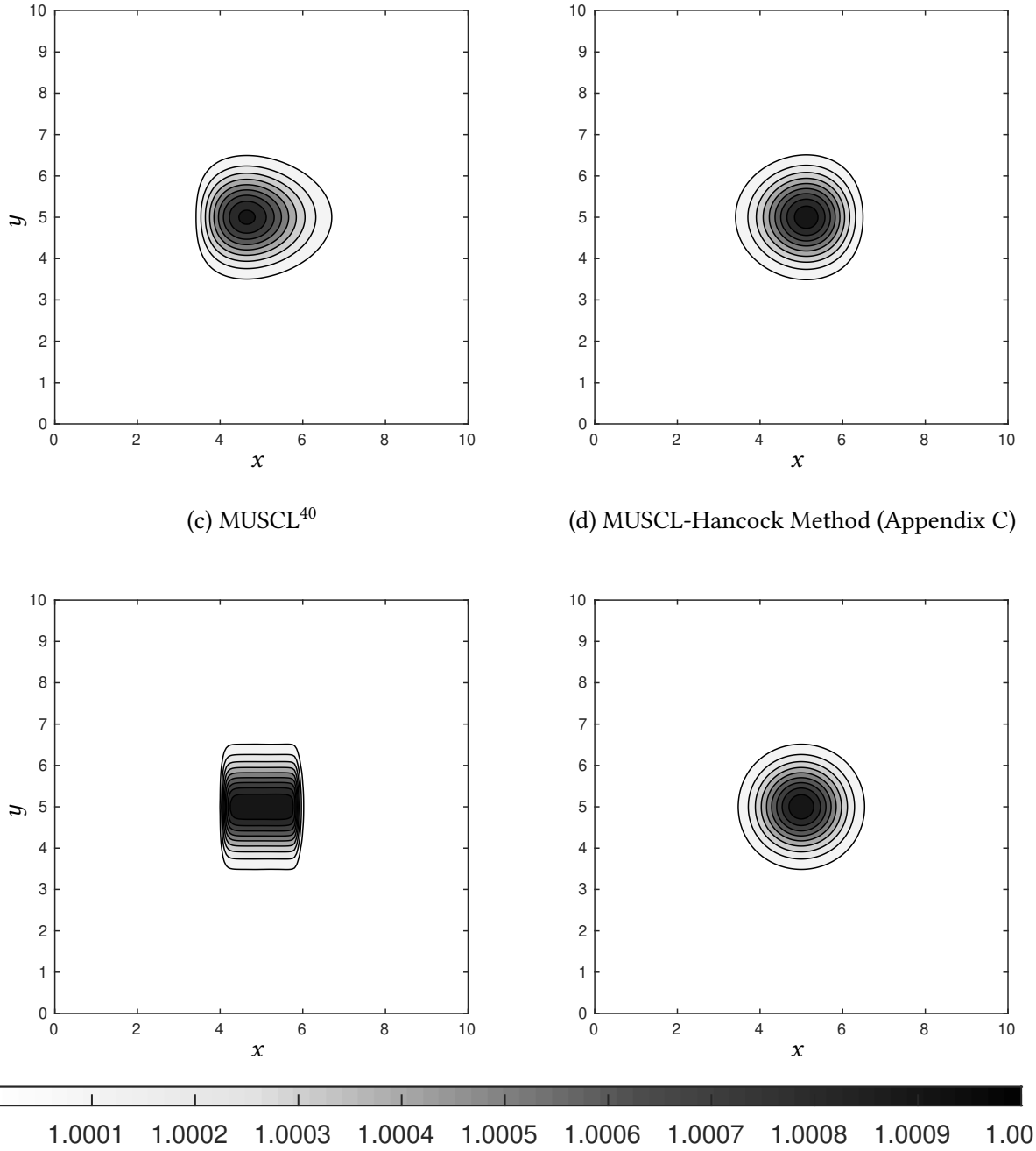

(c) MUSCL[40]

(d) MUSCL-Hancock Method (Appendix C)

Figure 5: Entropy spot : Comparison of density fields of the Ma = 1 advection after 20 periods for different discretizations of the convective term of Eq.(66).

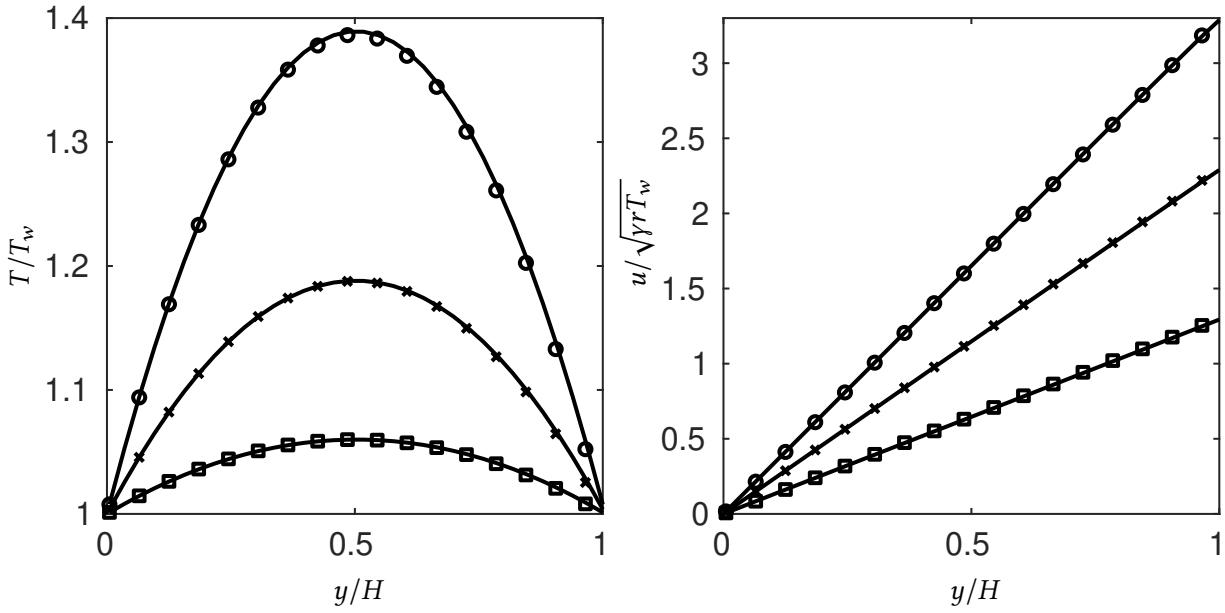

Figure 6: Thermal Couette flow : Left is normalized temperature, right is local Ma number. Squares, crosses and circles are the $Ma = 1.3,\ 2.3,\ 3.3$ references, solid lines correspond to numerical solutions with the present model.

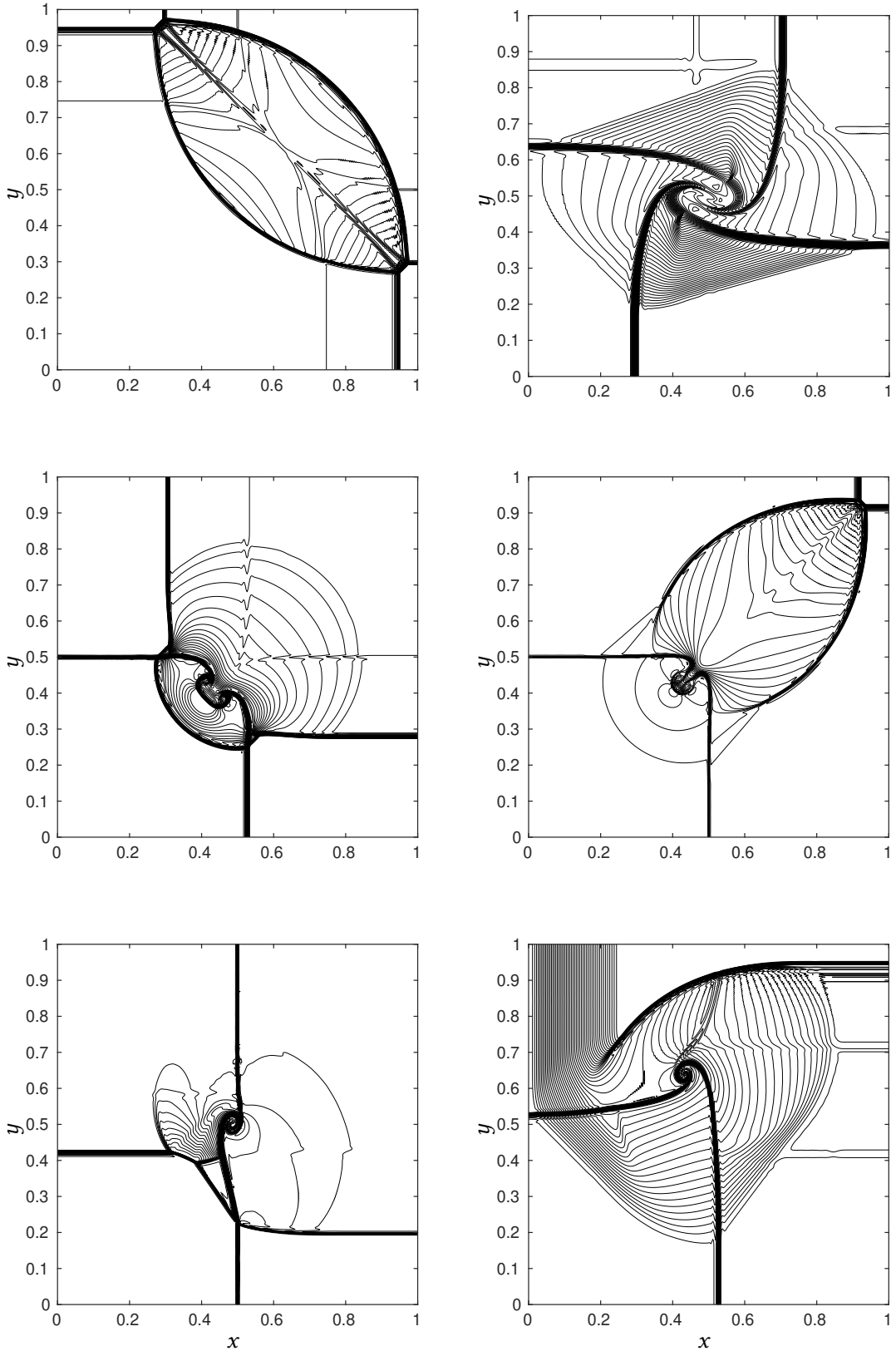

Figure 7: 2D Riemann problems : Density fields of configurations 4-6-11-12-13-16[43].

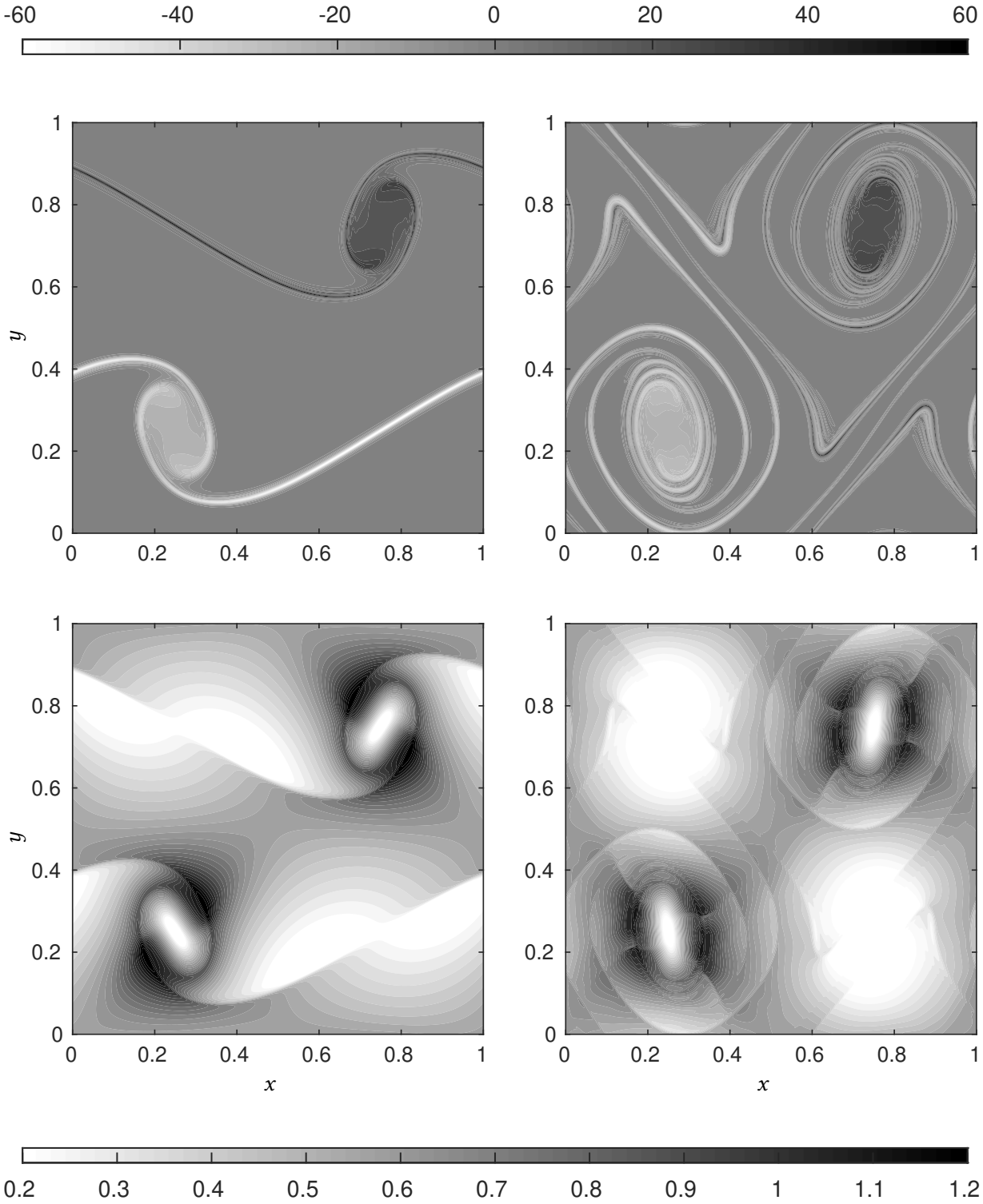

Figure 8: Double shear layer : Vorticity (top) and Mach (bottom) at time t_c (left) and $2t_c$ (right) using the 512×512 grid.

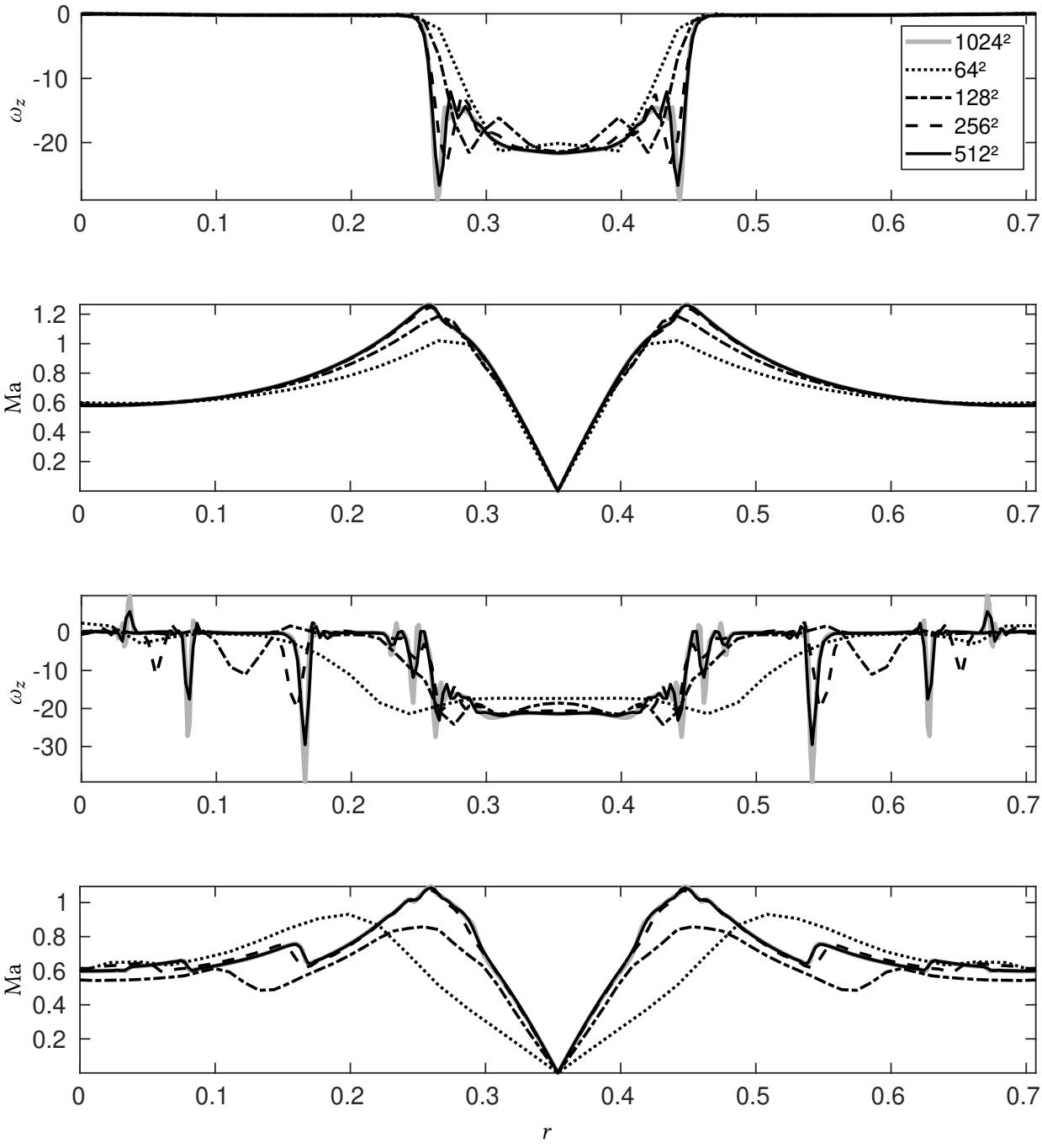

Figure 9: Double shear layer : Vorticity and Mach slices between points $(0, 0)$ and $(0.5, 0.5)$ at time t_c (top) and $2t_c$ (bottom) for different grid resolutions.

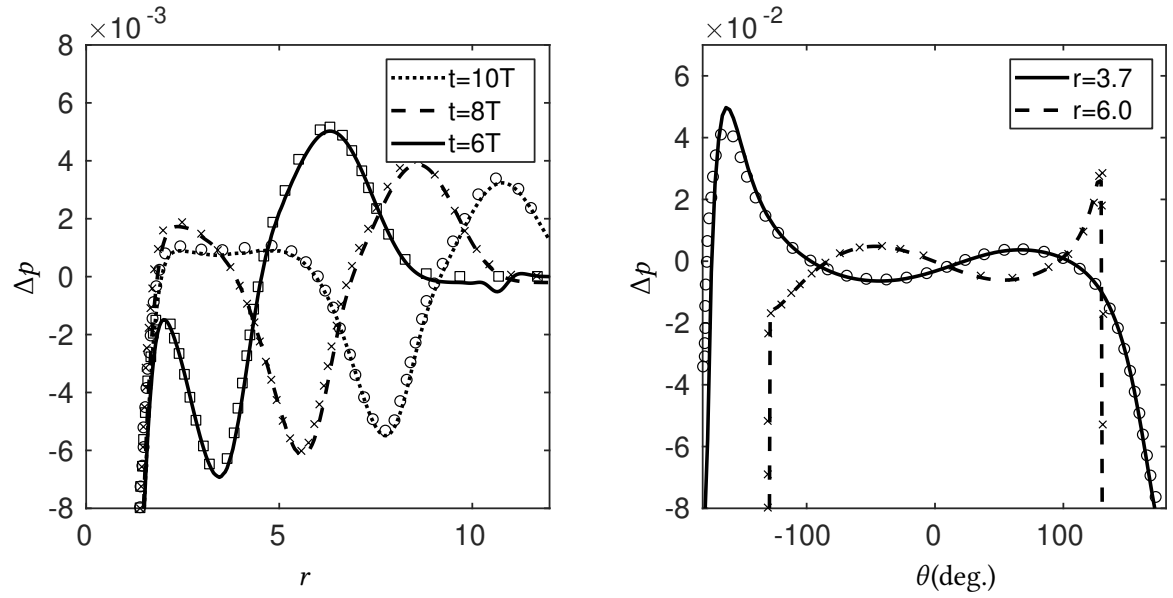

Figure 10: Vortex/shock interaction : Radial (left) and circumferential (right) cuts compared to reference[44] (symbols).

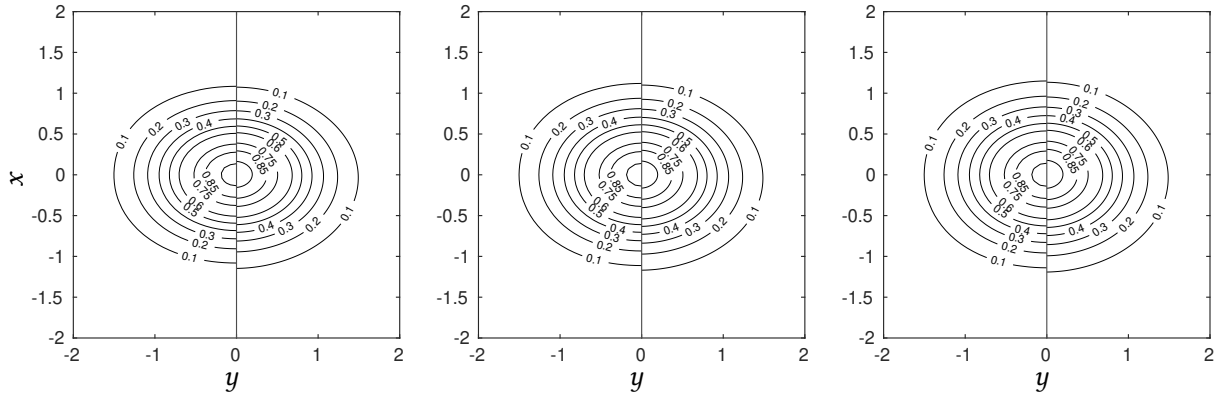

Figure 11: Entropy spot/shock interaction : Normalized transmitted entropy fields $s'/\epsilon C_p$, time $t = 8$. From left to right $\gamma = 1.2$, 1.4 and 1.6. Analytical[45,46] and numerical solutions respectively corresponds to $y < 0$ and $y \geq 0$ parts of the plot.

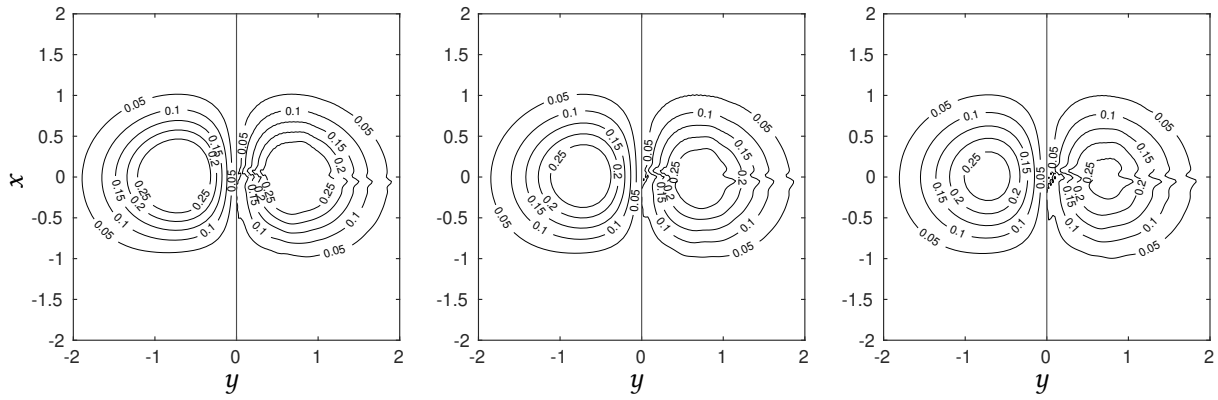

Figure 12: Entropy spot/shock interaction : Normalized transmitted vorticity fields $\omega' R/\epsilon u_0$, time $t = 8$. From left to right $\gamma = 1.2$, 1.4 and 1.6. Analytical[45,46] and numerical solutions respectively corresponds to $y < 0$ and $y \geq 0$ parts of the plot.

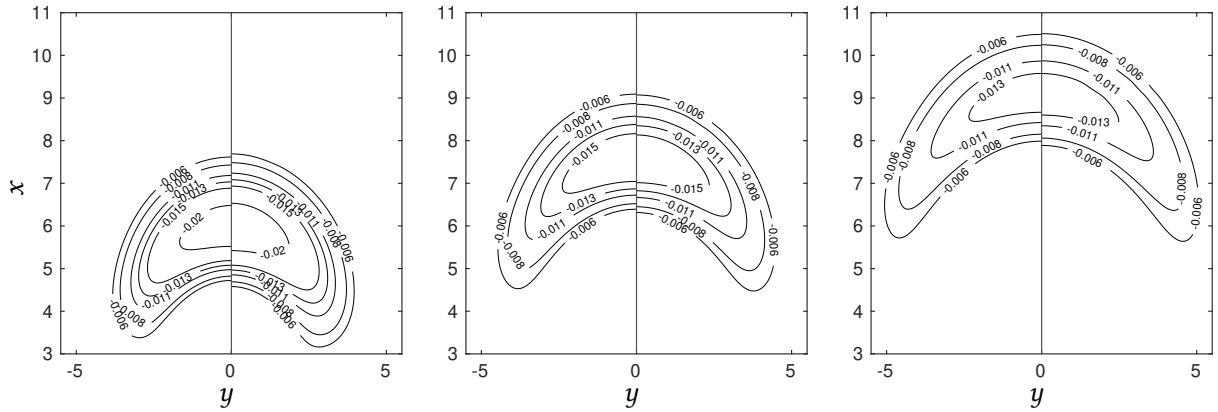

Figure 13: Entropy spot/shock interaction : Normalized transmitted pressure fields $p'/\epsilon\gamma p_0$, time $t = 8$. From left to right $\gamma = 1.2$, 1.4 and 1.6. Analytical[45,46] and numerical solutions respectively corresponds to $y < 0$ and $y \geq 0$ parts of the plot.